SDSS'Rio 2010 STABILITY AND DUCTILITY OF STEEL STRUCTURES
E. Batista, P. Vellasco, L. de Lima (Eds.)
Rio de Janeiro, Brazil, September 8 - 10, 2010

# LATEST DEVELOPMENTS IN THE GBT ANALYSIS OF THIN-WALLED STEEL STRUCTURES

**Dinar Camotim*, Cilmar Basaglia*, Rui Bebiano**, Rodrigo Gonçalves*** and Nuno Silvestre***

* Department of Civil Engineering and Architecture, ICIST/IST, Technical University of Lisbon, Portugal
e-mails: dcamotim@civil.ist.utl.pt, cbasaglia@civil.ist.utl.pt, nunos@civil.ist.utl.pt

** EST Barreiro, Polytechnical Institute of Setúbal, Barreiro, Portugal
e-mail: rui.bebiano@estbarreiro.ips.pt

*** Department of Civil Engineering, UNIC, Universidade Nova de Lisboa, Caparica, Portugal
e-mail: rodrigo.goncalves@fct.unl.pt

**Keywords**: Generalised Beam Theory (GBT), Thin-walled steel structures, First-order analysis, Buckling analysis, Post-buckling analysis, Vibration analysis, Dynamic analysis.

***Abstract***. *This work presents a state-of-the-art report of the most recent developments concerning formulations, numerical implementations and applications of Generalised Beam Theory (GBT) to analyse the structural response of thin-walled steel members and frames. After a brief overview of the cross-section analysis, one addresses new findings dealing with the use of GBT to assess the (i) first-order behaviour of steel-concrete composite bridge decks, (ii) buckling and post-buckling behaviour of members and frames with arbitrary loading and support conditions, (iii) vibration behaviour of load-free and loaded open-section members and (iv) dynamic behaviour of members subjected to periodic and moving loads. In order to illustrate the unique features and show the potential of the GBT approach, several numerical results are presented and discussed. For validation purposes, most of these results are compared with values yielded by shell finite element analyses, performed in the codes ADINA, ABAQUS and ANSYS.*

## 1 INTRODUCTION

Generalised Beam Theory (GBT) may be viewed as an extension of Vlasov's classical thin-walled bar theory that includes cross-section deformations (wall bending and distortion), thus combining the advantages of a one-dimensional formulation with the capability of folded-plate theory. It has been amply shown that GBT constitutes a rather powerful, elegant and clarifying method of structural analysis for prismatic thin-walled member and structures. Indeed the GBT approach offers possibilities not available when other numerical techniques, such as finite strip or (mostly) shell finite element analyses, are employed. This is due to the GBT unique features, which make it possible to decompose a member/frame deformed configuration or buckling/vibration mode into a linear combination of structurally meaningful "modal contributions". Such modal decomposition requires the identification of cross-section *deformation modes*, which is achieved through the performance of a special discretisation-and-orthogonalisation procedure designated as *cross-section analysis* – the "trademark" of GBT.

The pioneering work that led to the development of the GBT approach to perform structural analysis must be credited to Schardt [1], who subsequently was also responsible, together with his collaborators at the University of Darmsdadt, for the growth of GBT during about four decades. Another important contribution was due to Davies and co-workers [2-3], who (i) extensively employed GBT to investigate the local and global buckling behaviour of cold-formed steel profiles, and (ii) contributed decisively to disseminate it amongst the English-speaking technical-scientific community (the vast majority of the work carried out by Schardt *et al.* was only published in German). By the end of the last millennium, GBT was primarily used to perform elastic first-order and buckling analyses of thin-walled steel members with unbranched open cross-sections, namely cold-formed steel profiles (even if other structural analyses and cross-section shapes could already be handled by GBT [4]).

In the last decade, a research team at IST (Technical University of Lisbon) has devoted a very significant amount of research work to the development, numerical implementation, application and worldwide dissemination of novel GBT formulations that considerably broaden the scope of this theory, by enabling the performance of several additional analyses and covering a wider range of structural systems [5-7]. In particular, it is now possible to carry out (i) first-order, buckling, post-buckling, vibration and dynamic analyses of metal and FRP members with open and closed cross-sections, and (ii) first-order, buckling and post-buckling analyses of thin-walled steel frames.

The aim of this work is to report and provide a unified view on the most recent advances concerning the use of GBT analyses to assess the structural response of thin-walled steel members and frames. Besides presenting a brief (but insightful) overview of the fundamental concepts and main procedures involved in the performance of a GBT cross-section analysis, it (i) provides an account, illustrates the application and show the capabilities of several formulations that were developed and numerical implemented (beam finite elements) in the last couple of years, and also (ii) addresses the research work dealing with GBT that is currently under way. Due to space limitations and the large amount of material available, it is only possible to include a brief description of the new developments, followed by the presentation and discussion of illustrative numerical results – however, all the key references are provided, where the interested reader may find detailed accounts of all the work reported here. In particular, this paper is concerned with GBT formulations that can be applied to analyse the (i) first-order behaviour of steel-concrete composite bridge decks, (ii) buckling and post-buckling behaviour of members and frames exhibiting arbitrary loading and support conditions, (iii) vibration behaviour of load-free and loaded open-section members and (iv) dynamic behaviour of members subjected to periodic and moving loads. For the sake of validation and numerical efficiency assessment, most of the GBT-based results presented are compared with values yielded by shell finite element analyses carried out in commercial codes, namely ADINA [8], ABAQUS [9] and ANSYS [10].

## 2 CROSS-SECTION ANALYSIS

In order to obtain a displacement field representation compatible with the classical beam theory, GBT adopts the variable separation

$$u(x,s) = u_k(s)\phi_{k,x}(x) \qquad v(x,s) = v_k(s)\phi_k(x) \qquad w(x,s) = w_k(s)\phi_k(x) \quad , \quad (1)$$

where (i) $x$ and $s$ denote coordinates along the member length and cross-section mid-line, (ii) $u_k(s)$, $v_k(s)$ and $w_k(s)$ are functions providing the longitudinal, transverse membrane and transverse flexural displacements characterising deformation mode $k$, (iii) $(.)_{,x} \equiv d(.)/dx$, (iv) the summation convention applies to subscript $k$ and (v) $\phi_k(x)$ are mode amplitude functions defined along the member (or finite element) length.

Before carrying out a GBT structural analysis (*e.g.*, a first-order, post-buckling or vibration analysis) of a given thin-walled system (member or frame), one must begin by performing *cross-section analyses*, which provide the corresponding member "deformation modes" (*i.e.*, the functions $u_k(s)$, $v_k(s)$ and $w_k(s)$ appearing in eq. (1), which are the "essence" and "trademark" of GBT) and associated modal mechanical properties. This is achieved by means of specific discretisation-and-orthogonalisation procedures that vary with the cross-section type and were sequentially developed and reported in detail by (i) Silvestre and Camotim [11], Dinis *et al.* [12], Gonçalves *et al.* [13] and Silvestre [14, 15], in the context of buckling analysis, and by (ii) Silvestre and Camotim [16], for post-buckling analysis – it still worth noting the very recent work by Gonçalves *et al.* [17], which provides a very insightful and complete account on the determination of deformation modes in polygonal cross-sections.

In polygonal cross-sections (*i.e.*, excluding the circular and elliptical tubes investigated by Silvestre [14, 15]), it is possible to identify *two* main groups of deformation modes, involving (i) *conventional* (those originally considered by Schardt [1]) and (ii) *non-conventional* modes – the latter comprise *membrane shear*, *warping shear* and *transverse extension* modes. The main features of these various deformation mode sets are the following:

(i) The *conventional* modes, which are based on the null membrane shear strain and transverse extension assumptions, constitute the core of GBT and can still be subdivided into ($i_1$) *global* (cross-section in-plane rigid-body motions: axial extension, major/minor axis bending and torsion), ($i_2$) *distortional* and ($i_3$) *local* modes – the last two categories involve cross-section in-plane deformation (distortion and/or wall bending).

(ii) The *membrane shear* modes account for the membrane shear deformation occurring in walls belonging to

closed cells. They are obtained through the sequential imposition of unit membrane shear strains at each closed-cell wall ($\gamma^M=v_{,x}+u_{,s}=1$), while keeping null values at all the remaining (closed-section and open-branch) walls.

(iii) The *warping shear* modes make it possible to capture the *non-linear* variation of the warping displacements along the cross-section wall mid-lines. They are obtained by imposing unit warping displacements $u(s)$ and null membrane transverse displacements $v(s)$ at each (natural and intermediate) node – this procedure automatically implies null flexural displacements $w(s)$, *i.e.*, one has only $u(s)\neq 0$.

(iv) The *transverse extension* modes involve only in-plane displacements (*i.e.*, $u(s)=0$) and account for the cross-section deformation due to the wall membrane transverse extensions. They are obtained through the imposition of unit membrane transverse displacements $v(s)$ and null warping displacements $u(s)$ at each node – flexural transverse displacements $w(s)$, uniform along each wall mid-line, may be required to ensure transverse displacement compatibility at the natural nodes.

Non-conventional deformation modes were already included in recent GBT-based investigations. For instance, (i) Gonçalves and Camotim [18] considered warping shear modes to analyse the shear lag effects in twin-box girder bridges, (ii) Silvestre and Camotim [19] used warping shear and transverse extension modes to study the post-buckling behaviour of cold-formed steel lipped channel members, and (iii) Dinis *et al.* [20] utilised membrane shear modes to assess the buckling behaviour of cold-formed steel hollow-flange channel beams.

Figure 1 shows the geometries (shapes and dimensions) and possible GBT discretisations of most of the thin-walled member cross-sections dealt with in this work. Figures 2 to 5 depict the main features of the corresponding deformation modes that are more relevant for the analyses carried out in the paper (*i.e.*, those with significant contributions to the member buckling/vibration mode shape or first-order/post-buckling deformed configurations).

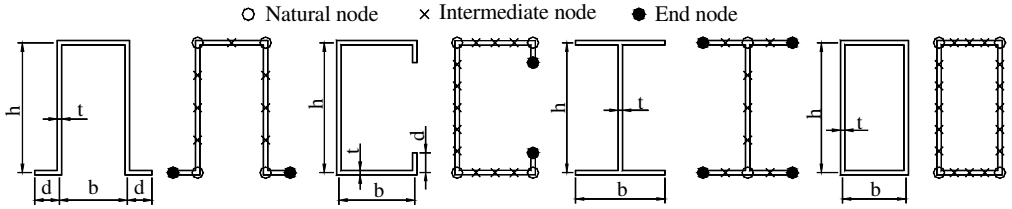


| Designation | Shape | Young's modulus (GPa) | Web *h* (*mm*) | Flange *b* (*mm*) | Lip *d* (*mm*) | Thickness *t* (*mm*) |
|---|---|---|---|---|---|---|
| HS120×60×2.0 | Hat-section | 210 | 120 | 60 | 20 | 2.0 |
| C100×40×1.0 | | 210 | 100 | 40 | 20 | 1.0 |
| C100×60×1.0 | Lipped | 205 | 100 | 60 | 5 | 1.0 |
| C100×100×2.0 | Channel | 200 | 100 | 100 | 20 | 2.0 |
| C202×75×2.3 | | 205 | 202 | 75 | 20 | 2.3 |
| I300×150×5.0 | I-section | 205 | 300 | 150 | - | 5.0 |
| RHS200×75×3.0 | RHS | 205 | 200 | 75 | - | 3.0 |

*Note: All the steel members dealt with in this work have mass density $\rho=7.85 g/cm^3$ and Poisson's ratio $\nu=0.3$.*

Figure 1: Hat-section, lipped channel, I-section and RHS dimensions and possible GBT discretisations.

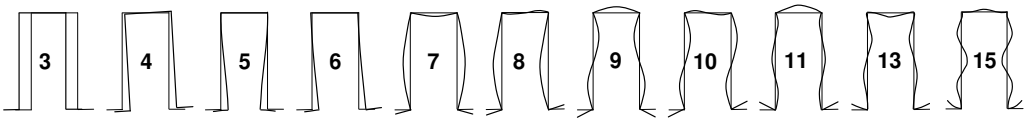


Figure 2: Main features of the most relevant hat-section deformation modes.

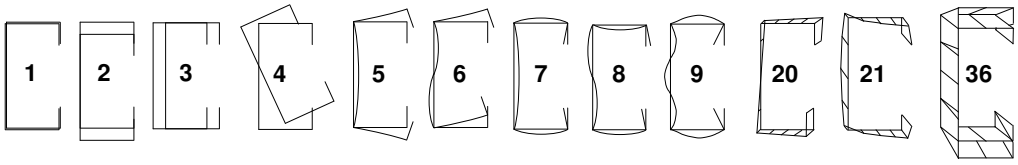


Figure 3: Main features of the most relevant lipped channel deformation modes.

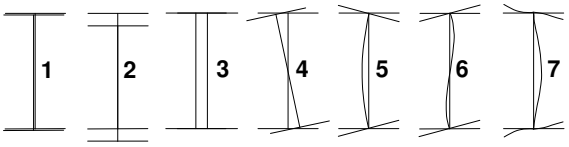


Figure 4: Main features of the most relevant I-section deformation modes.

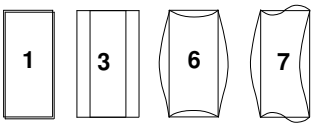


Figure 5: Main features of the most relevant RHS deformation modes.

## 3 FIRST-ORDER ANALYSIS

In the context of member first-order (geometrically linear) analysis, the GBT system of equilibrium equations (one per deformation mode), expressed in terms of the modal amplitude functions $\phi_k(x)$, is given by

$$C_{ik}\phi_{k,xxxx} - D_{ik}\phi_{k,xx} + B_{ik}\phi_k = q_h \quad , \quad (2)$$

where (i) $q_h$ are the modal applied loads and (ii) $C_{ik}$, $D_{ik}$ and $B_{ik}$ are cross-section modal mechanical properties, defined in [11, 18] – while $C_{ik}$ and $D_{ik}$ concern the warping displacements and torsional rotations, $B_{ik}$ stem from local deformations (wall bending and distortion).

Gonçalves and Camotim [18] have recently employed a novel GBT-based approach to analyse the first-order behaviour of steel-concrete composite beams and bridges (i) acted by eccentric vertical loads, causing bending and torsion, and (ii) having cross-sections that combine closed cells with open branches and exhibit displacement constraints to model box diaphragms. In order to illustrate this approach, let us consider the first-order behaviour of the simply supported (pinned end sections that may warp freely) steel-concrete composite twin-box girder bridge with (i) the cross-section geometry and dimensions given in figure 6(a), (ii) a 20m span and (iii) the material properties *E=37GPa*, *v=0.1* (C50/60 concrete deck) and *E=210GPa*, *v=0.3* (steel girders). The loading consists of a mid-span vertical force applied at point *A* (see fig. 6(a)), causing combined bending and torsion in the bridge – due to symmetry, only half of the bridge is analysed.

Concerning the cross-section analysis, the main challenge is to identify deformation modes that can easily accommodate the presence of box diaphragms at the bridge piers and/or along its span. This challenge is met by means of the auxiliary system depicted in figure 6(b), in which (i) the diaphragm constraint is modelled by a single cross-link (all walls are assumed inextensible) and (ii) rigid links fill the gap between the mid-lines of the concrete slab and steel girder top flanges. Then, the cross-section analysis leads to the following *13* deformation modes:

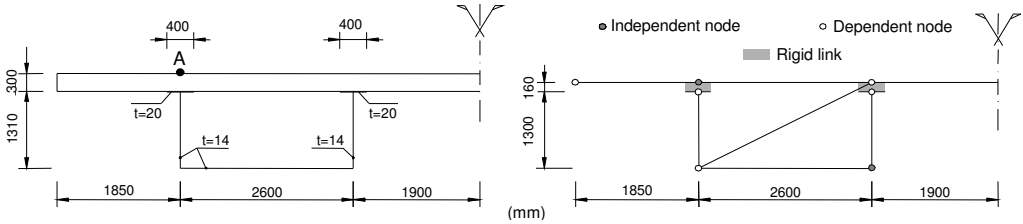


(a) (b)

Figure 6: Bridge cross-section (a) geometry and (b) GBT discretisation.

(i) *5* modes calculated assuming $u_x+v_x=0$ (**1**-**5**: axial extension, major/minor axis bending torsion and distortion) – see figure 7. The torsion mode (**4**) involves the combination with a closed-cell "shear flow" mode [17].

(ii) *2* modes due to the imposition a unit elongation at each cross-links: symmetric (**6**) and anti-symmetric (**7**) cross-link-induced distortion – see figure 7.

(iii) *6* membrane shear modes stemming from the imposition of unit membrane shear strains in each of the *6* steel closed-cell walls (**8**-**13** – see fig. 8) – the concrete deck is assumed rigid and rigidly attached to the top flanges.

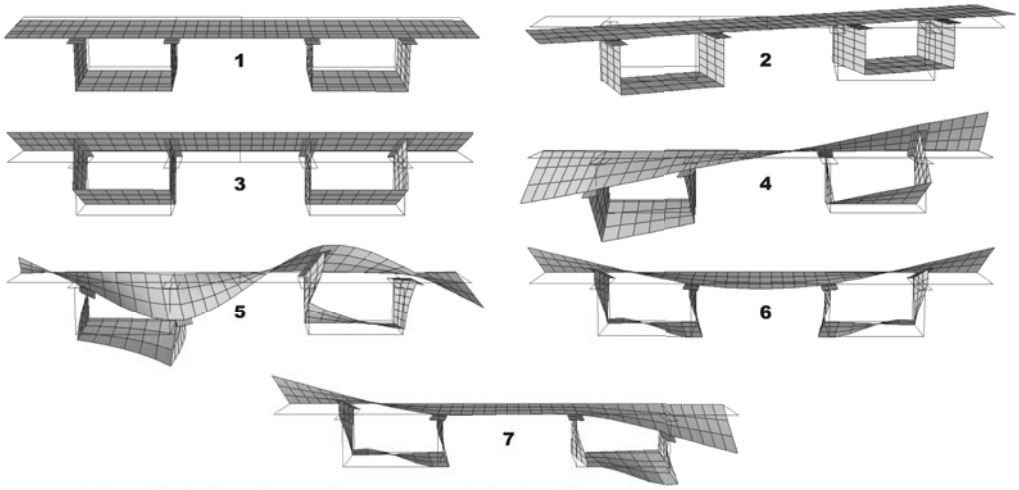


Figure 7: Deformation modes: conventional (**1**-**5**) and due to cross-link induced distortion (**6**-**7**).

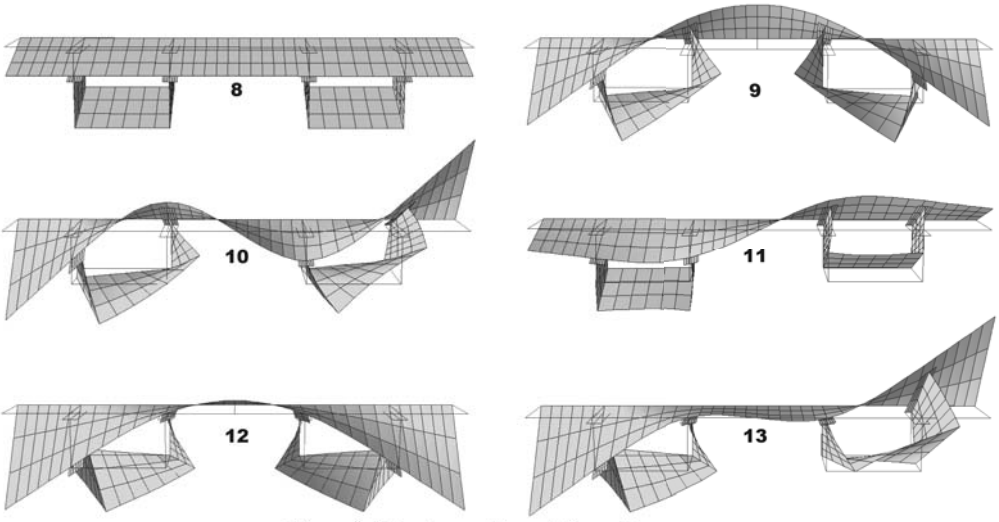


Figure 8: Membrane shear deformation modes.

Figures 9 and 10 show the deformed configurations of one half of the bridge with diaphragms located (i) at the piers and (ii) at the piers and mid-span – these configurations were yielded by (i) GBT-based beam finite element analyses (*3* equal-length elements) and (ii) ADINA shell finite element analyses (*4*-node element mesh). On the other hand, figures 11(a)-(b) and 12(a)-(b) show the variation of the vertical displacement (i) with the beam finite element number (at mid-span) and (ii) along the length (GBT values with *3* elements) for the two bridge configurations.

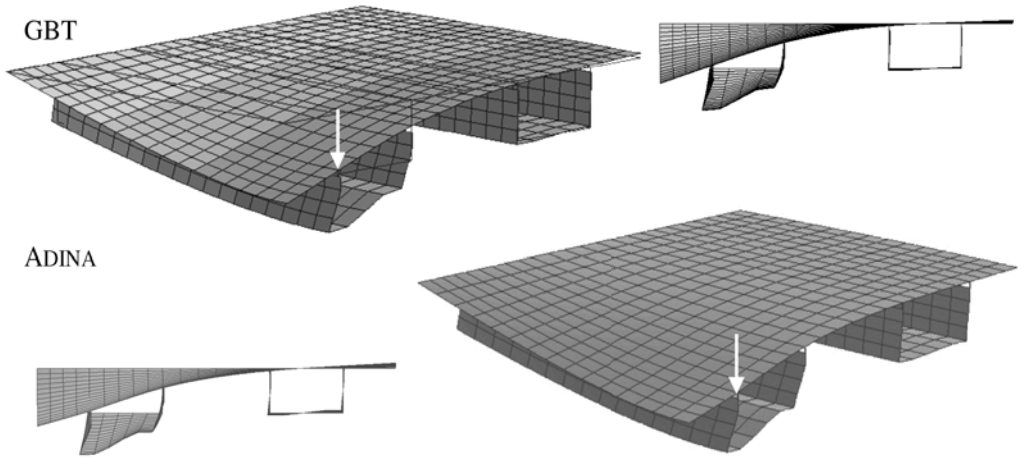


Figure 9: Deformed configurations of half of the bridge (diaphragms at the piers) ($\times 10^5$).

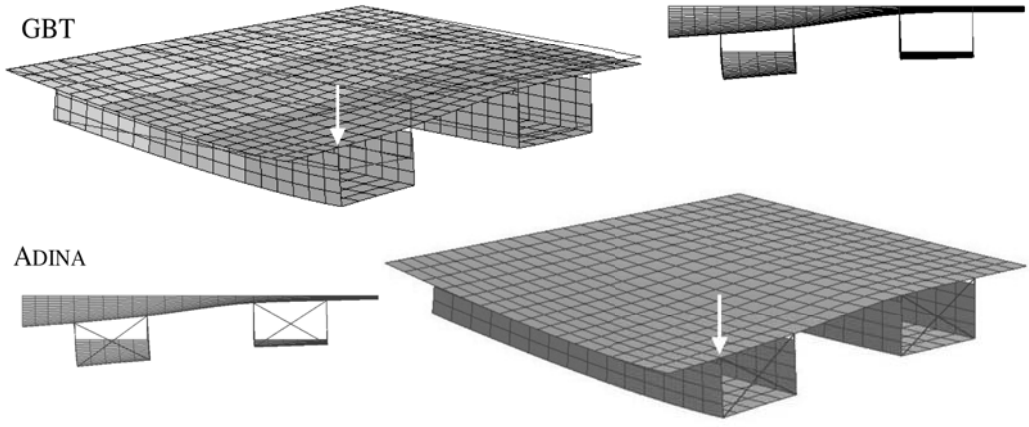


Figure 10: Deformed configurations of half of the bridge (diaphragms at piers and mid-span) ($\times 10^5$).

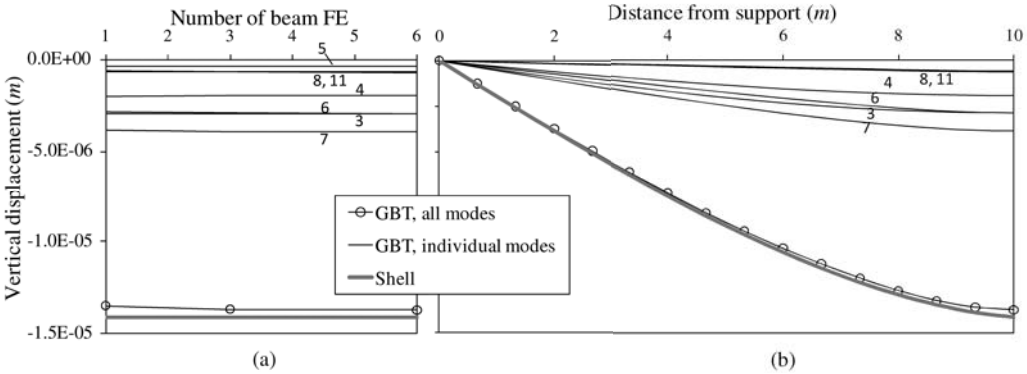


Figure 11: Variation of the vertical displacements (a) with the beam finite element number (at mid-span – point *A*) and (b) along the beam length (longitudinal line passing in *A*) – bridge with diaphragms at the piers.

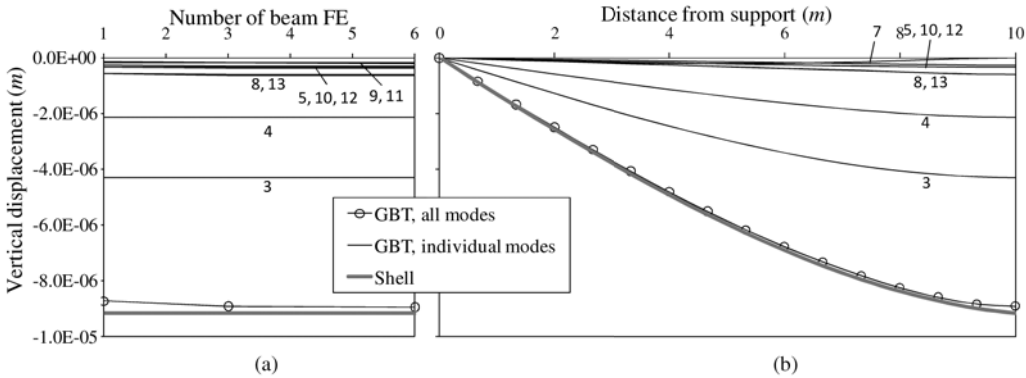


Figure 12: Variation of the vertical displacements (a) with the beam finite element number (at mid-span – point *A*) and (b) along the beam length (longitudinal line passing in *A*) – bridge with diaphragms at the piers and mid-span.

One notices that the GBT-based and ADINA results virtually coincide, even for a discretisation involving as little as *3* beam finite element – for this discretisation, displacement differences of *3.0%* (diaphragms at the piers) and *2.5%* (diaphragms at the piers and mid-span). Moreover, the GBT modal participations, shown in figures 11 and 12, provide valuable insight into the mechanics of the bridge structural response – no such detailed and structurally meaningful information can be extracted from the shell finite element results.

The GBT analysis may also account for the shear lag effects, by incorporating deformation modes associated with the non-linear variation of the warping displacements along cross-section wall mid-lines (warping shear modes) [18]. In this case, the deformation modes included in the analysis concerned the bottom flanges and consisted of single half-wave sinusoidal warping functions – modes **14** and **15** in figure 13(a). Figure 13(b) shows the normal stress distributions at the mid-span loaded cross-section half for the two bridge configurations – results yielded by (i) GBT analyses (*3* beam finite elements) including modes **1**-**13** and **1**-**15**, and (ii) the previous ADINA analysis. It is clear that including the "shear lag modes" makes it possible to capture the non-linearity of the lower flange stress distribution. Moreover, the GBT stresses match quite accurately the ADINA ones, even if one peak stress (*78.6kPa* – bottom right corner) is underestimated by about *17%* – additional deformation modes, namely *local* ones, would be required to obtain a more accurate peak stress.

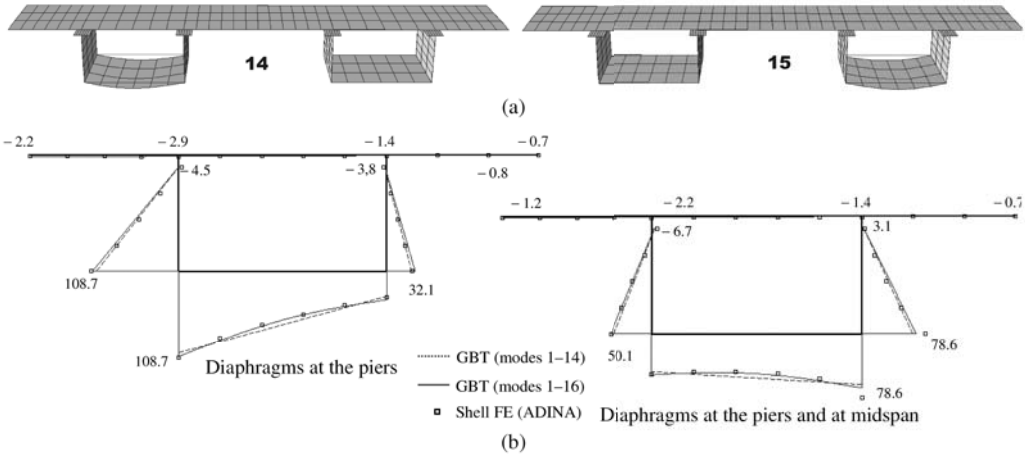


Figure 13: (a) Single half-wave shear lag deformation modes and (b) normal stress distributions (*kPa*) at the mid-span loaded cross-section half for the two bridge configurations (stress values indicated from the ADINA analysis).

## 4 BUCKLING ANALYSIS

The GBT system of equilibrium equations governing the member or frame buckling behaviour is given by

$$C_{ik}\phi_{k,xxxx} - D_{ik}\phi_{k,xx} + B_{ik}\phi_k - \lambda\left[X^{\sigma}_{jik}\left(W^0_j\phi_{k,x}\right)_{,x} - X^{\tau}_{jki}\left(W^0_{j,x}\phi_k\right)_{,x} + W^0_{j,x}X^{\tau}_{jik}\phi_{k,x}\right] = 0 \quad , \quad (3)$$

where (i) $\lambda$ is the load parameter and (ii) $X^{\sigma}_{jik}$ and $X^{\tau}_{jik}$ are geometric stiffness components associated with the pre-buckling normal stress resultants $W^0_j$ and shear stresses due to the longitudinal stress gradients, all defined in [21].

Concerning the buckling analysis of isolated members, Bebiano *et al.* [21] developed a GBT-based beam finite element formulation capable of analysing single-span beams with standard support conditions (*i.e.*, free, pinned or fixed end sections) acted by transverse loadings associated with major and/or minor axis bending. This formulation incorporates the geometric stiffness reduction due to non-uniform compression and/or major/minor axis bending, causing longitudinal normal stress gradients and shear stresses (varying bending moments). Soon after, Camotim *et al.* [22] extended the above GBT-based beam finite element, making it possible to assess the local, distortional and global buckling behaviour of thin-walled members with a wide variety of loading and support conditions, including intermediate and/or localised supports (simulating bracing systems or connectors). In order to incorporate these non-standard support conditions into the analysis, the system (3) must be solved subjected to *constraint conditions* that (i) vary from case to case and (ii) are expressed as linear combinations of the appropriate set of modal degrees of freedom (d.o.f.). A little later, Silva *et al.* [23] further improved the GBT buckling analysis capabilities, by incorporating into the beam finite element formulation geometric stiffness associated with *transverse* normal stresses, a feature enabling the capture of effects related to (i) patch loading (concentrated loads) and/or (ii) the application of transverse loads away from the cross-section shear centre (*e.g.*, loads applied at channel or I-beam top flanges).

As far as thin-walled frames are concerned, the major difficulties in applying GBT (or any other beam model) lie in the appropriate treatment of the joints, which involves the simultaneous consideration of (i) the warping transmission due to torsion and/or distortion and (ii) the compatibility between the transverse (membrane and flexural) displacements of the connected member end sections – moreover, it also convenient to be able to simulate the connections/restraints stemming from the presence of bracing systems. To overcome these difficulties, a GBT-based beam finite element approach was developed and numerically implemented. This approach makes it possible to assess the buckling behaviour of thin-walled plane and space frames (i) built from RHS or open cross-section members, (ii) having localised supports stemming bracing systems, (iii) exhibiting various joint configurations and (iv) acted by loadings causing non-uniform internal force and moment diagrams. This work is mostly due to Basaglia [24] and a fairly complete state-of-the-art report was recently published by Camotim *et al.* [7].

### 4.1 Illustrative examples

In this sub-section, numerical results concerning the buckling behaviour of (i) hat-section cantilevers [23], (ii) a cold-formed RHS portal frame [25] and (iii) a restrained space frame [26] are presented and discussed. For validation purposes, most GBT-based critical buckling loadings and mode shapes are compared with values yielded by shell finite element analyses carried out in ABAQUS [9] or ANSYS [10] – the cantilevers and frames are discretised into refined S9R5 (ABAQUS) and SHELL181 (ANSYS) element meshes, respectively.

#### 4.1.1 Hat-section cantilevers

One analyses the buckling behaviour of HS120×60×2.0 cantilevers acted by two identical transverse point loads applied at either the end-section web-flange or web-lip corners – $Q$ is the total applied load. The main objective is to assess the influence of the load position on the cantilever critical buckling moment ($M_{cr}$=$Q_{cr}$.$L$) and mode shape. Figures 14(a)-(b) and 15 show, for the two loadings considered, (i) $M_{cr}(L)$ buckling curves, (ii) the corresponding GBT modal participations diagrams and (iii) the GBT-based critical buckling mode shapes concerning cantilevers with three lengths. The observation of these buckling results prompts the following remarks:

(i) There is an excellent agreement between all the GBT and ABAQUS critical moments – differences below *4%*.

(ii) There is a clear difference between the cantilever critical buckling moments and mode shapes associated with the top and bottom loadings. Concerning the $M_{cr}$ values, those corresponding to bottom loading may exceed by more than *300%* their top loading counterparts (see fig. 14(a)). In both cases, the critical buckling modes include

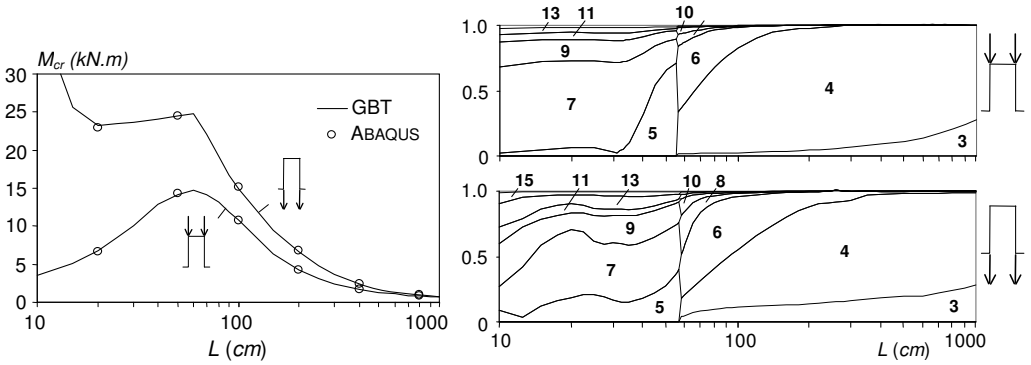


Figure 14: Hat-section cantilevers: (a) $M_{cr}(L)$ buckling curves and (b) GBT modal participation diagrams concerting the two position of the tip point loads.

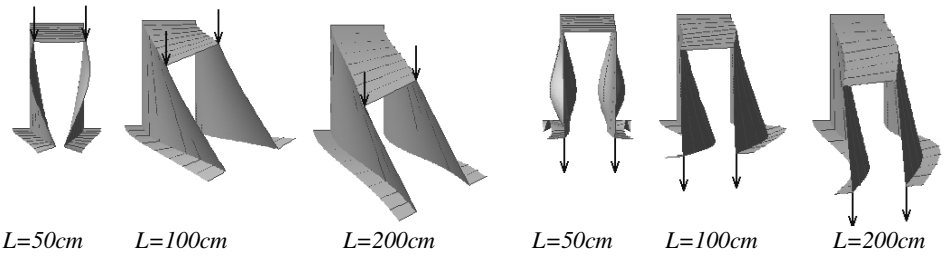


Figure 15: Hat-section cantilevers: GBT-based critical buckling mode shapes for three lengths and the two loadings under consideration.

relevant contributions from global, distortional and local deformation modes, as shown in figures 14(b) and 15 – they combine ($ii_1$) symmetric distortional (**5**) and local (**7**, **9**, **11**, **13**, **15**) modes, for $L<55$ *cm*, or ($ii_2$) anti-symmetric global (**3**, **4**), distortional (**6**) and local (**8**, **10**) modes, for $L>55$ *cm*.

(iii) Figure 15 shows the critical buckling modes of three cantilevers ($L=50$ *cm*, $L=100$ *cm* and $L=200$ *cm*) under top and bottom loading. In order to illustrate the statements made in the previous item, consider the $L=100$ *cm*, for which one has ($iii_1$) $M_{cr}=10.67$ *kN.m* and *14.84 kN.m* (*39%* increase), and ($iii_2$) the "replacement" of contribution of torsion (mode **4** – *80.2-43.9%* decrease) by those of distortion and minor axis bending (modes **6** and **3** – *15.9-40.5%* and *2.4-11.2%* increases) – see figures 14(a)-(b).

### 4.1.2 RHS plane frame

Next, one investigates the buckling behaviour of the symmetric portal frame depicted in figure 16, (i) formed by three orthogonal RHS200×75×3.0 members (*A*, *B*, *C* – frame in-plane behaviour corresponding to minor axis bending), (ii) with fixed column bases and (iii) subjected only to axial compression (equal loads *P* applied at the joints). Figure 17 provides ANSYS and GBT-based 3D representations of the buckled frame joint region – note that the GBT view is obtained from a *beam* finite element analysis. Figure 18 displays, for each frame member, the amplitude functions of the two deformation modes that participate in the frame critical buckling mode. The comparison between the buckling results yielded by the two numerical models leads to the following comments:

(i) The two critical loads obtained virtually coincide: $P_{cr.GBT}=370.3kN$ and $P_{cr.ANSYS}=381.3kN$ (*2.9%* difference). However, note the disparity between the d.o.f. numbers: *648* (GBT – *80* finite elements) and *22600* (ANSYS).

(ii) There is also a close agreement between the GBT modal amplitude functions and the ANSYS buckling mode shape – they providing different representations of a well defined local buckling mode. However, it can easily be argued that the GBT result enables a better quantitative and qualitative grasp of the frame buckling mechanics.

(iii) The frame critical buckling mode is anti-symmetric and involves the three members: it exhibits *12* half-waves in each column and *6 half-waves* in the beam. Only the local deformation modes **6** and **7** have visible contributions to the frame critical buckling mode, with a clear dominance of mode **6** (note that the mode **7** contribution is amplified ten times). The more relevant (local) deformations occur in the column central regions and, as expected, the beam deformations are noticeably smaller.

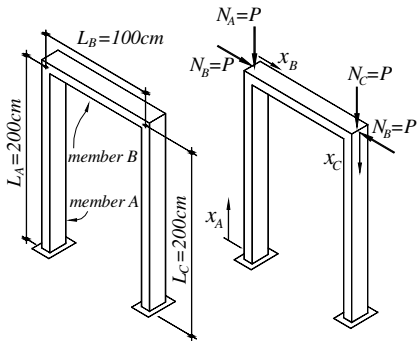


Figure 16: RHS portal frame geometry, loading and support conditions.

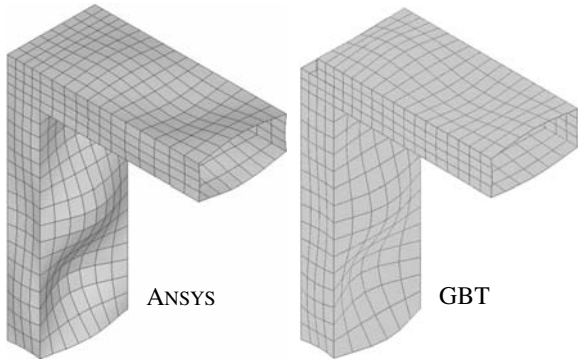


Figure 17: ANSYS and GBT views of the buckled frame joint region.

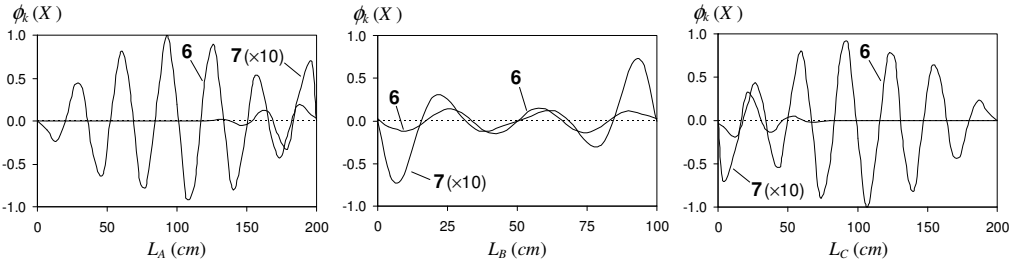


Figure 18: RHS portal frame – member modal amplitude functions $\phi_k(X)$.

4.1.3 I-section space frame

Finally, the buckling analysis of the symmetric space frame depicted in figure 19(a) is presented and discussed. This frame (i) comprises two portal frames (*F1* and *F2*) joined by a transverse beam (*TB*), all built from I300×150×5.0 members, and (ii) is acted by five equal vertical loads (*P*) applied at the four column tops and at the centroid of the transverse beam mid-span cross-section. All column-to-beam joints are box-stiffened (web continuity) and the beam-to-beam ones exhibit flange continuity. Moreover, (i) the column bases are fixed, (ii) the transverse displacement along $\overline{X}$ is prevented at all column-to-beam joints (see fig. 19(b)) and at the *TB* mid-span cross-section, and (iii) the displacement along $\overline{Z}$ is prevented at all column-to-beam joints ("rigid" diagonal and transversal tie-rods, connected to I-section mid-web point – see also fig. 19(b)).

Figures 20(a) and 20(b) show (i) the GBT modal amplitude functions for column *A* and beams *B* and *TB*, and (ii) a 3D view of the frame critical buckling mode shape, yielded by the ANSYS shell finite element analysis (tie-rod modelled with a *6cm* and BEAM189 elements). As before, the GBT analysis requires only a small fraction of the d.o.f. involved in its ANSYS counterpart: *1030* (*80* beam elements – *8* per column and *16* per beam) versus *25000*. The following conclusions can be drawn from the comparison between these two sets of frame buckling results:

(i) The GBT and ANSYS critical loads are again extremely close: $P_{cr.GBT}=161.83kN$ and $P_{cr.ANSYS}=159.11kN$ (*1.71%* difference). Moreover, there is an excellent correlation between the ANSYS buckling mode shape and the GBT modal amplitude functions. This assessment can by further (and amply) confirmed by looking at figure 20(c), providing ANSYS and GBT 3D views of the buckled *TB* mid-span region.

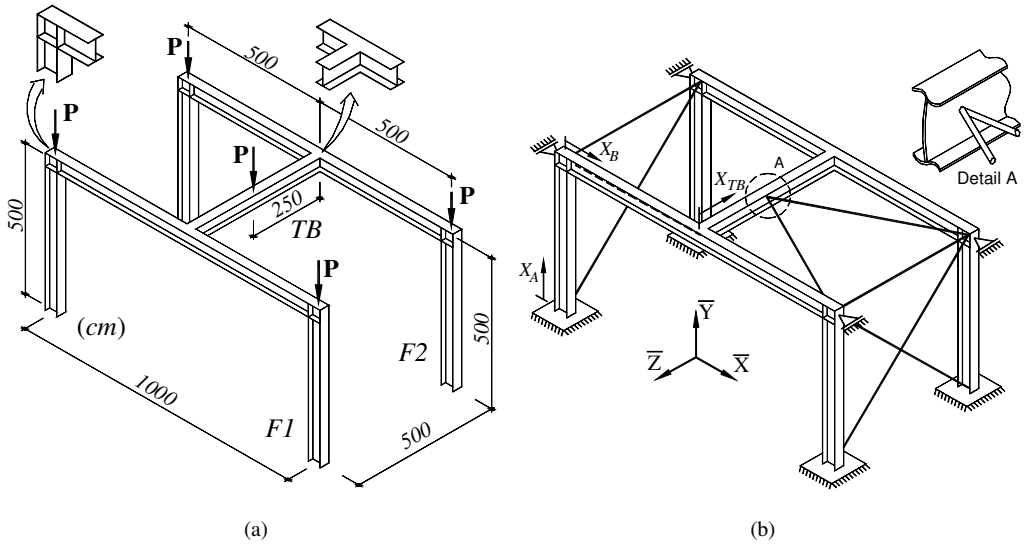


(a) (b)

Figure 19: Space frame (a) geometry and loading, and (b) support conditions and transverse beam bracing detail.

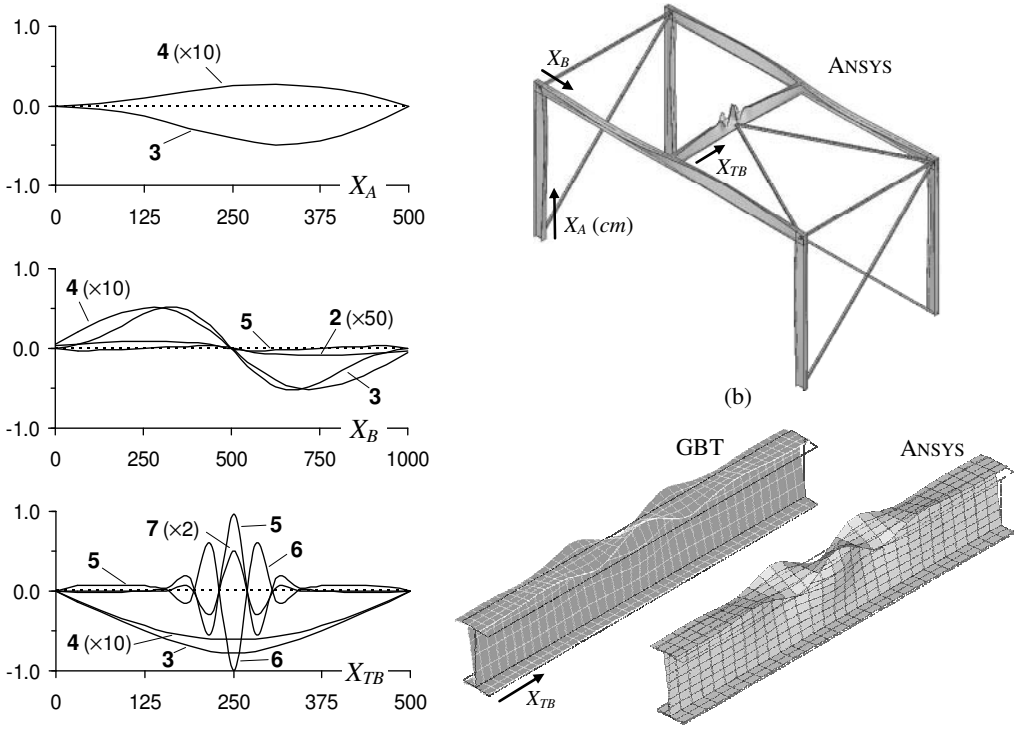


(a) (b) (c)

Figure 20: (a) GBT and (b) ANSYS space frame critical buckling mode representations, and (c) *TB* mid-span region buckled shapes.

(ii) The frame critical buckling mode is triggered by the *TB* and combines participations from global (**3**, **4**) and local (**5**, **6, 7**) deformation modes. While the latter occur mainly in the beam mid-span region (higher bending moments), the influence of the former is felt along the whole beam length – due to small wall thickness, the occurrence of local buckling hamper the bracing system efficiency in preventing lateral-torsional buckling.

(iii) The portal frame members experience mostly lateral-torsional buckling (maximum values near the beam 1/4 and 3/4-span cross-sections) – in the beams, there are also minute contributions from modes **2** and **5**.

## 5 POST-BUCKLING ANALYSIS

The determination of a member/frame post-buckling behaviour involves solving the one-dimensional problem governed by the system of non-linear differential equilibrium equations

$$C_{kh}(\phi_k-\bar{\phi}_k)_{,xxxx}-D_{kh}(\phi_k-\bar{\phi}_k)_{,xx}+B_{kh}(\phi_k-\bar{\phi}_k)-C_{kh}(\phi_k-\bar{\phi}_k)_{,xxxx}+\tfrac{1}{2}C_{hjk}(\phi_{k,x}\phi_{j,x}-\bar{\phi}_{k,x}\bar{\phi}_{j,x})_{,xx}+ \\ +\tfrac{1}{2}C_{kijh}(\phi_{k,x}\phi_{i,x}\phi_{j,x}-\bar{\phi}_{k,x}\bar{\phi}_{i,x}\bar{\phi}_{j,x})_{,x}+h.o.t.=q_h \quad , \quad (4)$$

where the bar identifies the modal amplitude functions defining the initial geometrical imperfections. While the second-order tensor components ($C_{kh}$, $D_{kh}$, $B_{kh}$) characterise the member linear (first-order) behaviour, the third ($C_{kijh}$, etc.), fourth ($C_{kijh}$, etc.) and higher-order (*h.o.t.*, not shown in (4)) ones are associated with its geometrically non-linear behaviour – all these tensor components are given in [16, 27].

In isolated members, the solution of the non-linear system (4) can be obtained by means of a GBT-based beam finite element formulation developed and implemented by Silvestre and Camotim [16], in the context of unbranched open-section members, and recently extended by Basaglia *et al.* [27] to cover members with arbitrary open cross-sections (*i.e.*, including also branched ones) and allow for the consideration of non-standard support conditions, such as localised displacement restraints (*e.g.*, those stemming from bracing) or intermediate supports.

The most recent GBT developments are due to Basaglia *et al.* [28, 29] and concern a geometrically non-linear GBT formulation applicable to assess the local, distortional and global post-buckling behaviour of thin-walled frames. It incorporates arbitrary initial geometrical imperfections (expressed in *modal* form) and is able to handle the kinematics of joints connecting two non-aligned members, namely those associated with the compatibility between the connected cross-section warping (due to axial extension, bending, torsion, distortion and/or shear) and transverse (due to overall flexure, wall bending and transverse extension) displacements and rotations. As in the case of isolated members, the numerical solution of the discretised system of non-linear algebraic equilibrium equations is obtained by means of an incremental-iterative technique based on Newton-Raphson's method and adopting either a load or a displacement control strategy.

### 5.1 Illustrative examples

This sub-section includes numerical results concerning the post-buckling behaviours of (i) a laterally restrained lipped channel beam [30] and (ii) a symmetric portal frame [28], both containing critical-mode initial geometrical imperfections. As before, the GBT beam finite element results are compared with values yielded by shell finite element analyses – in this case, carried out in ANSYS and adopting discretisations into SHELL181 element meshes.

#### 5.1.1 Laterally restrained lipped channel beam

The beam analysed is simply supported, has length $L=200cm$, exhibits a C202×75×2.3 cross-section, is acted by a uniformly distributed load $q$ applied at the shear centre axis and is laterally restrained by means of two pairs of rigid supports located at the web-flange corners (see detail in fig. 21) of its 1/3 and 2/3-span cross-sections.

The first step consists of determining the beam buckling behaviour. Figure 21 provides representations of the beam critical buckling mode provided by the ANSYS (3D view) and GBT (modal amplitude functions $\phi_k(x)$) analyses – the corresponding buckling loads are $q_{cr.ANSYS}=0.664\ kN/cm$ and $q_{cr.GBT}=0.671\ kN/cm$ (*1.05%* difference). It is also worth noting that, due to the lateral restraints, only distortional (**5**+**6**) and local (**7**+**8**) deformation modes have perceptible contributions to the beam buckling mode – as expected, the maximum participations of these modes occur in the beam mid-span region.

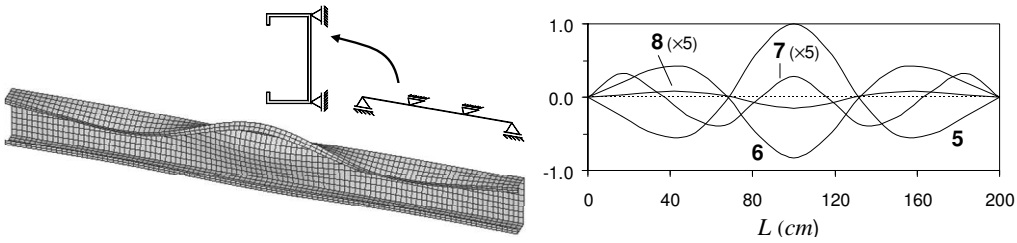


Figure 21: ANSYS and GBT representations of the restrained beam critical buckling mode shape.

The post-buckling analysis performed involves a beam containing critical-mode initial imperfections with amplitude $v_0 = -0.02cm$, where $v$ is the mid-span flange-lip corner vertical displacement – see fig. 22(a). Figure 22(a) shows the equilibrium paths ($q$ vs. $v$) yielded by the shell (ANSYS) and beam (GBT) finite element analyses. The modal participation diagram of figure 22(b) provides information about the evolution of the "relative participations" of the various GBT deformation modes to the beam deformed mid-span cross-section along the post-buckling equilibrium path. After observing these post-buckling results, one is led to the following conclusions:

(i) A virtually "exact" beam post-buckling equilibrium path is provided by a GBT analysis that includes only deformation modes **1+2+5-8+20+21+36** – for $v<5.0cm$, the differences between the GBT and ANSYS equilibrium paths are always below *3.5%*. Moreover, note that the GBT analyses involve only a small fraction of the number of degrees of freedom required by the ANSYS ones: *168* against over *12500*.

(ii) Major axis flexure (mode **2**) governs the early loading stages and is progressively "replaced" by distortional (modes **5**+**6**) and local (**7**) deformation as the applied load increases.

(iii) The modal participation diagram shows that the contributions of modes **5** and **6-8** decrease until they reach null values, for $q=0.107\,kN/cm$ and $q=0.278kN/cm$, and then gradually increase again. This fact stems from the predominance of major axis flexure (mode **2**), which "forces" modes **5-8** to invert their amplitude signs – *i.e.*, forces the upper flange-lip assembly to move downwards (the initial imperfection made it move upwards).

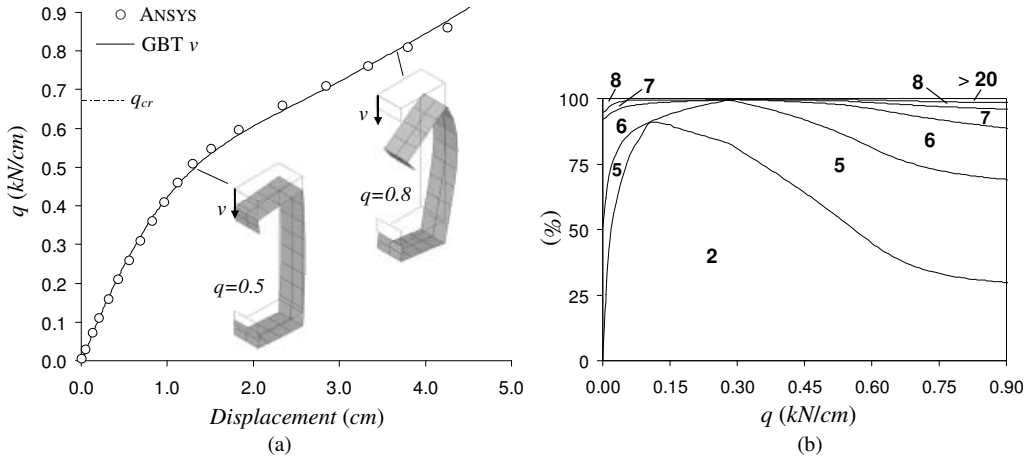


Figure 22: Restrained beam (a) post-buckling equilibrium paths and two mid-span cross-section deformed configurations (ANSYS – × 2), and (b) modal participation diagram concerning the mid-span cross-section.

Figure 23 shows the beam deformed configuration and longitudinal normal stress distribution for $q=0.5kN/cm$, both yielded by the GBT analysis. Note that (i) there is an excellent correlation between the ANSYS and GBT-based mid-span cross-section deformed configuration (see fig. 22(a)), and (ii) high compressive and tensile stresses occur at the beam central third-length, involving the whole width of the top and bottom flanges, respectively.

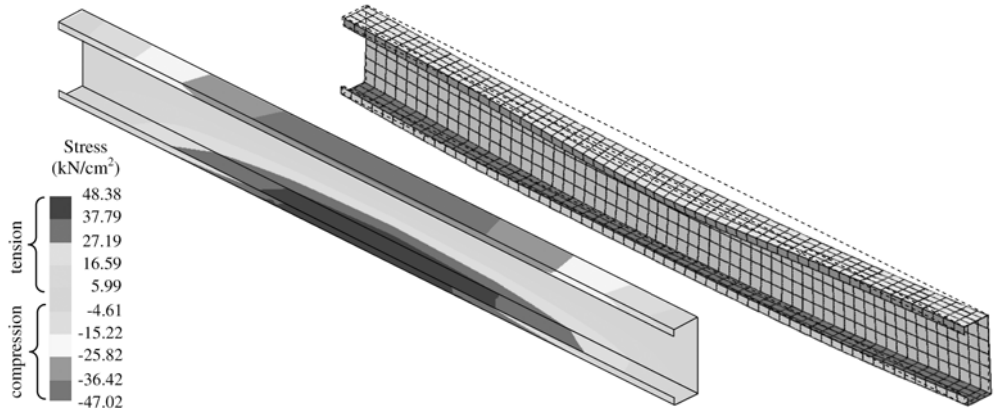


Figure 23: Restrained beam GBT 3D deformed configuration and normal stresses ($q$=*0.5 kN/cm*).

5.1.2 Lipped channel portal frame

Finally, one presents the analysis of post-buckling behaviour of the symmetric portal frame depicted in figure 24, which (i) is formed by three equal length ($L$=*70cm*) C100×60×1.0 members (columns $A$ + $C$, and beam $B$), (ii) has fixed column bases and unstiffened joints with flange continuity, and (iii) is subjected exclusively to uniform axial compression ($N_A$=$N_C$=$P$ and $N_B$=*1.2P*). Note that this (unrealistic) frame geometry was carefully selected to ensure a high susceptibility to both local and distortional deformations/buckling.

Figure 25 shows the results of the frame buckling analysis: ANSYS (3D view) and GBT (modal amplitude functions in column $A$ and beam $B$) representations of the critical buckling mode shape, which correspond to $P_{cr,ANSYS}$=*14.68kN* and $P_{cr,GBT}$=*14.34kN* (*2.32%* difference). The frame buckles in "mixed" local-distortional mode that (i) involves the three members and (ii) includes contributions from deformation modes **5** (distortional) and **7+9** (local) – although mode **5** is highly dominant (*75.3%*), with the maximum values occurring at the beam $B$ mid-span region, there are also non-negligible contributions from modes **7** and **9** in the joint vicinities.

Figure 26 shows post-buckling equilibrium paths involving the transverse displacements ( $v_{\bar{Y}}$ ) of (i) the member $A$ and $B$ mid-span flange-lip corners (points $R_1$ and $R_3$) and (ii) the intersection of the flange-lip longitudinal edges at

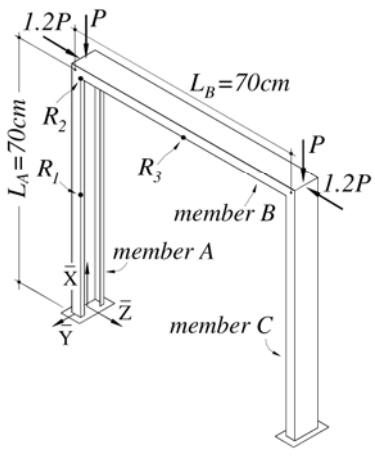


Figure 24: Symmetric portal frame: geometry and loading.

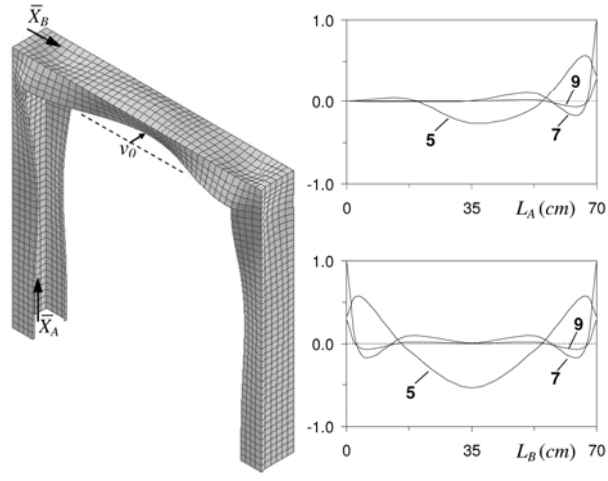


Figure 25: Frame critical buckling mode: 3D view (ANSYS) and column $A$ and beam $B$ modal amplitude functions (GBT).

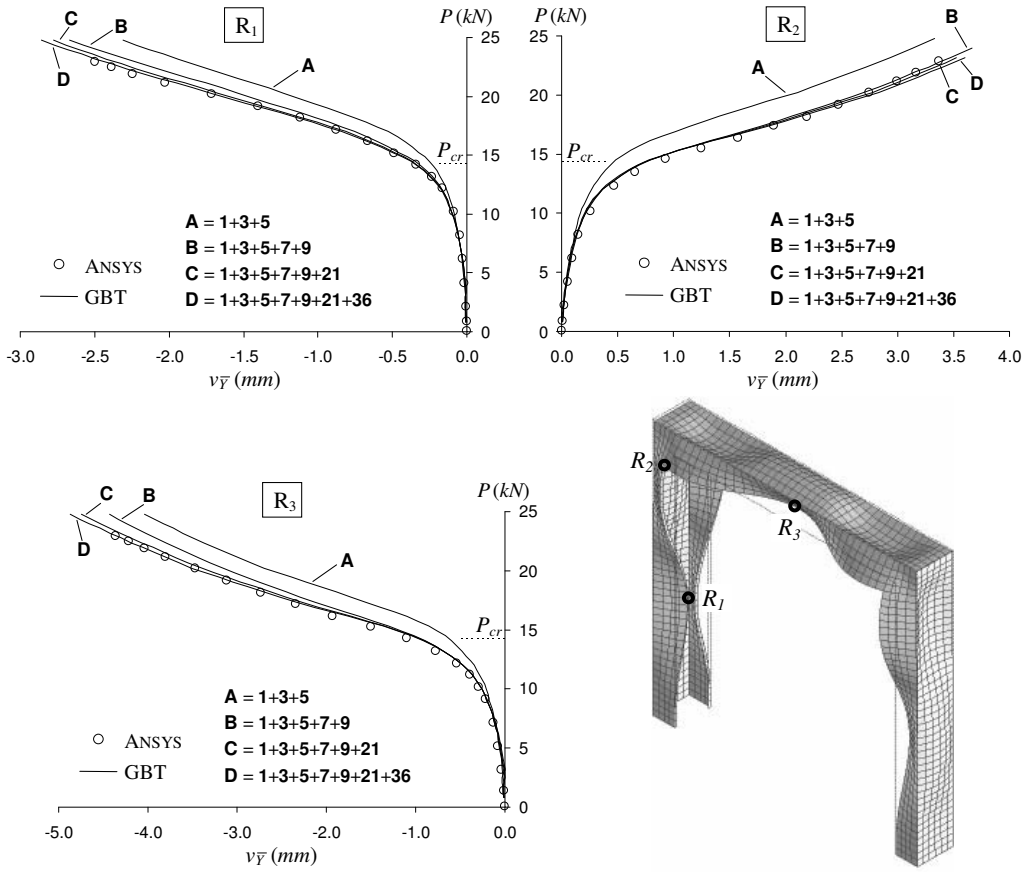


Figure 26: Frame equilibrium paths $P$ vs. $v_{\bar{Y}}$ (points $R_1$, $R_2$, $R_3$) and ANSYS deformed configuration ($P=23kN$).

the joint (point $R_2$) – this figure also includes the ANSYS deformed configuration at $P=23kN$. The frame contains critical-mode initial geometrical imperfections with amplitude $v_0=-0.15mm$ ($v_0$ is the beam initial $v_{\bar{Y}}$ value – *inward* flange-lip motions). Note that the GBT results presented were obtained with four different deformation mode sets. After comparing these beam (GBT) and shell (ANSYS) finite element post-buckling results, one concludes that:

(i) The "simpler" GBT analysis (only modes **1**+**3**+**5**) provides $v_{\bar{Y}}$ values that are very accurate up to $P\cong 10kN$ (*i.e.*, $P/P_{cr}\cong 0.7$). The accuracy is gradually eroded as $P$ increases, particularly in the beam – *e.g.*, for $P=P_{cr}$ the GBT $v_{\bar{Y}}$ values may underestimate the "exact" (ANSYS) ones by as much as *40%*.

(ii) The sole addition of the local modes **7**+**9** leads to accurate results up to about $P=P_{cr}$. At more advanced post-buckling stages, the GBT model becomes stiffer than the ANSYS one – *e.g.*, for $P=23kN$ (*i.e.*, $P/P_{cr}=1.6$) GBT provides a $v_{\bar{Y}}$ value at point $R_3$ that is *10%* above the "exact" one.

(iii) Further adding the warping shear mode **21** considerably improves the accuracy of the results, as the differences between the GBT and ANSYS values become quite small over the whole applied load range – the maximum discrepancy concerns point $R_1$ (column *A*), where the "exact" $v_{\bar{Y}}$ values is underestimated by *4.5%*.

(iv) Finally, including the transverse extension mode **36** in the analysis leads to virtually coincident GBT and ANSYS post-buckling equilibrium paths – even if the maximum difference is almost the same (*4.0%* for point $R_2$ and $P=1.6P_{cr}$), there is clear improvement in accuracy brought about by the inclusion of this mode.

(v) Given the similarity between the frame ($v_1$) critical buckling mode shape, displayed in figure 25, and ($v_2$) deformed configuration, shown in figure 26, one may conclude it that the frame retains (at least qualitatively) its

buckling deformation pattern throughout the whole post-buckling range (up until $P=1.6P_{cr}$).

(vi) Lastly, note once more the very high computational efficiency of the GBT approach: its more "heavy" implementation (*7* deformation modes and *24* beam finite elements – *8* per member) involves *346* degrees of freedom, against the more than *12500* required to perform a similarly accurate ANSYS analysis.

## 6 VIBRATION ANALYSIS

The system of differential equations to analyse the vibration behaviour of load-free or non-uniformly loaded isotropic members reads

$$\begin{aligned} &C_{ik}\phi_{k,xxxx} - D_{ik}\phi_{k,xx} + B_{ik}\phi_k - \omega^2\left(R_{ik}\phi_k - Q_{ik}\phi_{k,xx}\right) - \\ &- X_{jik}\left(W_j^0\phi_{k,x}\right)_{,x} + X_{jki}^{\tau}\left(W_{j,x}^0\phi_k\right)_{,x} - W_{j,x}^0 X_{jik}^{\tau}\phi_{k,x} = 0 \end{aligned} \quad , \quad (5)$$

where (i) $\omega$ are the member *natural frequencies* and (ii) $R_{ik}$ and $Q_{ik}$ are mass components that are given in [31] and account for the influence of the inertia forces on the *out-of-plane* and *in-plane* cross-section displacements – these tensor components include both translational and rotational inertia forces. The solution of this eigenvalue problem is again obtained by means of a GBT-based beam finite element, developed and implemented by Bebiano *et al.* [31], who then employed it to analyse the vibration behaviour of simply supported C100×40×1.0 beams subjected to a uniformly distributed transverse load applied along the shear centre axis – maximum bending moment $M$, taken as a fraction $\alpha$ of its critical value ($M=\alpha M_{cr}$). The most important aspects of this analysis are presented next.

When investigating the vibration behaviour of a loaded member, it is necessary to begin by studying its buckling and free vibration behaviours. Figures 27(a)-(b) show the corresponding GBT modal participation diagrams composition for beam lengths in the range *10<L<1000cm*, and also the ANSYS critical buckling and fundamental vibration mode shapes of the *L=100cm*. These buckling and vibration results show that:

(i) For *10 <L<80cm*, the beam critical buckling basically combine the local modes **7**-**10**, even if non-negligible participations of the distortional modes **5** and **6** appear for *L>30cm* and grow steadily up to *L≈80cm*. Inside the *80<L<130cm* range modes **7**-**9** govern and for *L>130cm* modes **3**+**4** are clearly predominant.

(ii) The fundamental vibration mode shape is predominantly ($ii_1$) *local* (mode **7**) for *L<25cm*, ($ii_2$) *distortional* (mode **5**, but relevant contributions from modes **3** and **7**) for *25<L<120cm*, ($ii_3$) *flexural-torsional-distortional* (modes **2**, **4** and **6**), for *120<L<400cm*, and ($ii_4$) *purely flexural* (mode **3**), for *L>400cm*.

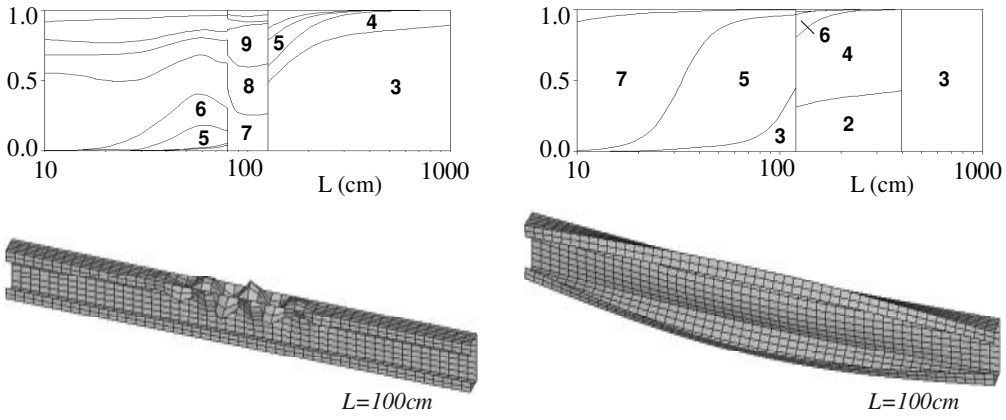


(a) (b)

Figure 27: Beam (a) critical buckling (uniformly distributed load) and (b) fundamental free vibration modes.

The curves in figure 28(a) provide the variation of the fundamental frequencies $\omega_{j,0}$ ($\alpha=0$ – load-free member) and $\omega_{j,\alpha}$ ($\alpha\neq0$ – members with eight $M$ levels) with $L$. Moreover, figure 28(b) shows the modal participation

diagrams of beams with three of those $\alpha$ values. The observation of these results prompts the following remarks:

(i) The load only causes noticeable fundamental frequency drops for $\alpha \geq 0.25$. Within the $0.5 < \alpha < 0.95$ range, the frequency drop rate increases significantly. Moreover, for $\alpha \geq 0.90$ the curves no longer decrease monotonically – they exhibit more or less pronounced upward branches at short-to-intermediate length ranges.

(ii) Severe fundamental frequency drops (*88%* and *86%*) occur for $110 \leq L \leq 145cm$ – within this length range, the vibration mode changes abruptly from ($ii_1$) local (**7**-**9**) with *25* half-waves to ($ii_2$) flexural-torsional-distortional (**3**-**6**) with a single half-wave, *i.e.*, a much more flexible configuration. In order to confirm this particular behaviour, the three ANSYS values included in figure 28(a) were determined – an excellent agreement was found, both in frequency values and vibration mode shapes (not shown here).

(iii) The comparison between the modal participation diagrams for $\alpha=0$ (see fig. 27(b)) and $\alpha=0.1$ shows that, unlike the $\omega_\alpha$ value, the fundamental vibration mode shape may be considerably altered by the presence of even quite small applied moments – in fact, either the distortional mode **6** joins modes **5**+**7** (intermediate beams) or the global mode **3** join modes **2**+**4** (longer beams – they are totally separated for $\alpha=0$).

(iv) Inside the $0.1<\alpha<0.95$ range, ($iv_1$) modes **8**-**10** gradually replace mode **7** (short beams), ($iv_2$) the contributions of modes **5** and **6** become closer (intermediate beams) and ($iv_3$) the relevance of mode **2** gradually fades (longer beams). Finally, for $\alpha>0.95$ the vibration mode shapes change quite drastically, approaching their critical buckling mode counterparts – indeed, for $\alpha=0.999$ the beam fundamental vibration and critical buckling modes virtually coincide throughout the whole length range, as attested by the comparison with figure 27(a).

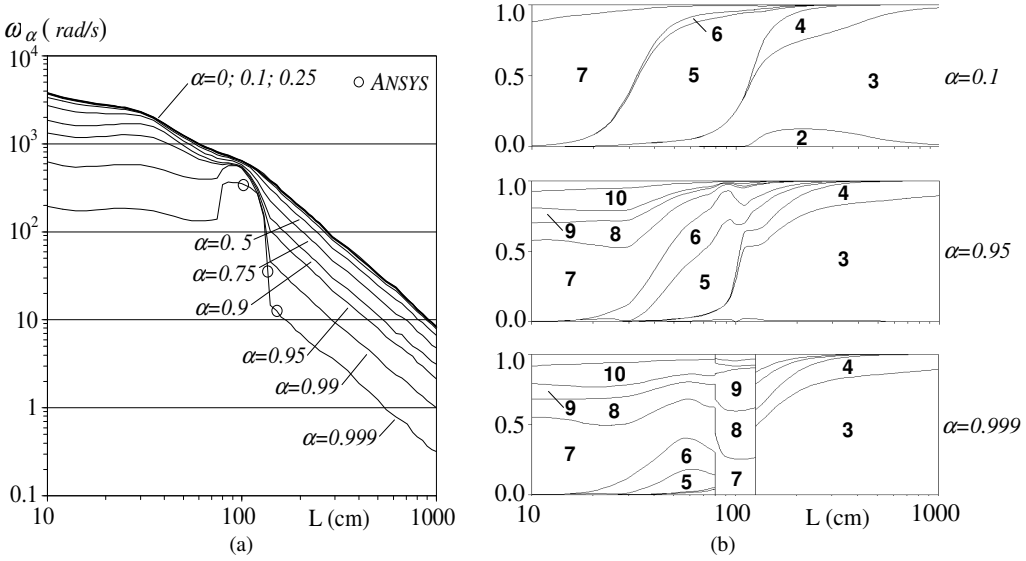


Figure 28: Variation of the fundamental (a) frequency $\omega_\alpha$ and (b) vibration mode participation diagram with $L$ ($\alpha=0.0$, *0.95* and *0.999*).

## 7 DYNAMIC ANALYSIS

Quite recently, Bebiano *et al.* [32] and Bebiano [33] developed a GBT formulation to analyse the local, distortional and global dynamic behaviour of open-section thin-walled members, which combines (i) the GBT modal discretisation with (ii) the classical Vibration Mode Superposition Principle (*e.g.*, [34]. This approach yields an original "doubly modal" displacement field representation that provides in-depth insight on the mechanics involved in the member dynamic response. The main concepts and procedures associated with this GBT formulation are briefly described and commented next:

(i) The system of GBT differential equilibrium equations describing the member dynamic behaviour is written as

$$C_{ik}\zeta_{k,xxxx} - D_{ik}\zeta_{k,xx} + B_{ik}\zeta_k - Q_{ik}\zeta_{k,xxtt} + R_{ik}\zeta_{k,tt} - q_i\varphi = 0 \quad , \quad (6)$$

where (i) $\zeta_k(x,t)$ are mode amplitude functions varying along the member axis and with time $t$, (ii) $q_i$ is the load resultant acting at a cross-section (obtained through the integration over its mid-line) and (iii) function $\varphi(x,t)$ describes the variation of this load resultant with the cross-section location and time.

(ii) The first step of solving (6) by means of the Vibration Mode Superposition Principle consists of determining the member (free) vibration mode shapes, which are the solution of the vibration eigenvalue problem defined by

$$C_{ik}\phi_{kj,xxxx} - D_{ik}\phi_{kj,xx} + B_{ik}\phi_{kj} - \omega_j^2(R_{ik}\phi_{kj} - Q_{ik}\phi_{kj,xx}) = 0 \quad , \quad (7)$$

where function $\phi_{kj}(x)$ provides the amplitude of the contribution of deformation mode $k$ to the member vibration mode $j$, corresponding to the natural frequency $\omega_j$. The solution of (7) may be obtained ($ii_1$) analytically, for pinned members, or ($ii_2$) numerically (GBT-based finite element), for members with other support conditions.

(iii) Then, the above vibration mode shapes are used as *coordinates* to represent the member dynamic response, *i.e.*, the solution of (6) – $\zeta(x, t)$. This solution is expressed as a linear combination of components of the form

$$\zeta_k(x,t) = \phi_{kj}(x)Y_j(t) \quad , \quad (8)$$

where ($iii_1$) function $Y_j(t)$ describes the time evolution of the component akin to vibration mode $j$ and ($iii_2$) $j$ varies between *1* and the number of vibration modes incorporated in the dynamic analysis ($n_v$). The number and nature of such components depends on the particular GBT cross-section discretisation adopted and also on which subset of $n_d$ deformation modes are considered in the analysis.

(iv) In order to determine the $n_v$ functions $Y_j(t)$, thus completely characterising the member dynamic response, it is necessary to solve the differential equation system

$$Y_{j,tt}(t) + \omega_j^2 Y_j(t) = \varphi_j^*(t) \quad , \quad (9)$$

where $\varphi_j^*(t)$ is the generalised load associated with the (vibration) modal coordinate $j$, whose determination depends on whether the vibration eigenvalue problem (7) is solved analytically or numerically. This system comprises $n_v$ uncoupled equations and, for most loadings, can be solved by means of standard analytical or numerical methods available in the literature.

(v) The member displacement field can finally be expressed as a product of functions of $(x,s)$ and $t$ – one has

$$u(x,s,t) = \{\ [\Phi]_x\ ]\{Y\} \qquad v(x,s,t) = \{\ [\Phi]\ \}\{Y\} \qquad w(x,s,t) = \{\ [\Phi]\ \}\{Y\} \quad , \quad (10)$$

where ($v_1$) the $1\times n_d$ vectors $\{\mathbf{u}\}$, $\{\mathbf{v}\}$ and $\{\mathbf{w}\}$ contain the GBT deformation mode shapes $u_k(s)$, $v_k(s)$ and $w_k(s)$, ($v_2$) the $n_d\times n_v$ matrix $[\Phi]$ components $\phi_{kj}(x)$ are longitudinal amplitude functions providing the contributions of each GBT deformation mode to each vibration mode, and ($v_3$) the $n_v\times 1$ vector $\{Y\}$ comprises the vibration mode evolution functions $Y_j(t)$**.** Since (10) involves both GBT deformation modes and vibration modes, it may be viewed as a *doubly modal* representation of the member dynamic response. It is possible to identify the individual contribution of a given ($v_1$) deformation mode (participating in several vibration modes) or ($v_2$) vibration mode (involving several deformation modes) to the member overall dynamic response.

### 7.1 Illustrative examples: lipped channel beams

One analyses the dynamic behaviour of a simply supported (locally and globally pinned end section that may warp freely) C100×100×2.0 steel beam with length $L=100cm$ and acted by (i) a uniformly distributed transverse load $q_z=0.01kN/cm^2$, applied on the web with a periodic (sinusoidal) time variation, and (ii) a point transverse load $Q_z=1.0kN$, moving longitudinally (constant speed $c$) along the beam mid-web segment – see figures 29(a)-(b). The time-dependencies of these loads are described by the functions $\varphi(t)=\sin(\Omega t)$ and $\varphi(x,t)=\delta(x-ct)$, where (i) $\Omega$ is the angular frequency and (ii) $\delta$ is the Dirac delta function.

#### 7.1.1 Preliminary vibration analysis

Table 1 presents the results of the lipped channel beam free vibration analysis, required to assess the beam dynamic response by means of the Mode Superposition Principle. It includes information concerning the first *10*

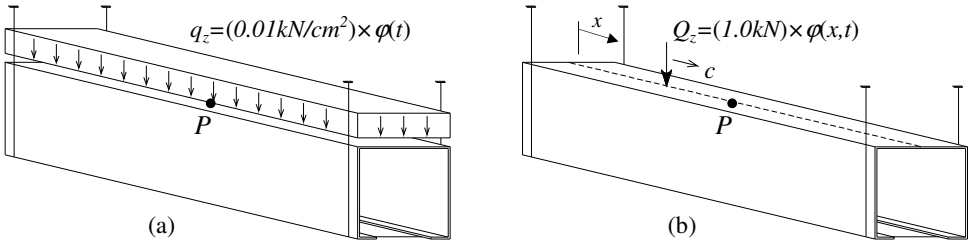


Figure 29: Lipped channel dynamic loadings: (a) uniformly distributed load and (b) moving point load.

vibration modes, namely (i) the natural (angular) frequency values $\omega_j$, obtained by means of GBT and ANSYS (shell finite element) analyses, (ii) the relative differences $\Delta(\%)$ between them, (iii) the number of longitudinal half-waves $n_j$ and (iv) the modal participation factors $mp_k(\%)$. Due to the symmetry of the loadings (with respect to the member major plane), only *symmetric* (odd-numbered) deformation modes were included in the GBT analysis, which implies that the vibration mode orders are different in the GBT and ANSYS analyses (see the first and third columns of table 1) – the latter yields both symmetric (odd-numbered) and anti-symmetric (even-numbered) vibration mode shapes. Note also that, when analysing the beam acted by the uniformly distributed transverse load, only the vibration modes with *odd* half-wave numbers (*i.e.*, longitudinally symmetric) need to be considered: the ***1st***, ***3rd***, ***4th***, ***6th***, ***8th*** and ***10th*** (GBT) vibration modes, whose mid-span cross-section deformed configurations are shown in figure 30.

Table 1 shows that the $\omega_j$ values yielded by the GBT (*8* d.o.f.) and ANSYS (*6341* d.o.f.) analyses are almost identical – the higher differences concern the ***3rd*** and ***4th*** (GBT) vibration modes and are equal to *3.11%* and *1.49%*. In spite of these small $\Delta$ values, it will be shown later that, in the particular cases dealt with here, the $\omega_j$ difference has a non-negligible impact on the beam dynamic response.

Table 1: GBT and ANSYS beam free vibration analysis – ten first natural frequencies and vibration modes.

| GBT | | ANSYS | | $n_j$ | $\Delta(\%)$ | Modal Participations (%) | | | | | | | |
|---|---|---|---|---|---|---|---|---|---|---|---|---|---|
| Mode | $\omega_j$ (*rad/s*) | Mode | $\omega_j$ (*rad/s*) | | | $mp_3$ | $mp_5$ | $mp_7$ | $mp_9$ | $mp_{11}$ | $mp_{13}$ | $mp_{15}$ | $mp_{17}$ |
| ***1st*** | 582.8 | *1st* | 582.2 | 1 | 0.11 | 0.58 | 98.15 | 1.01 | 0.22 | 0.02 | 0.02 | 0.00 | 0.00 |
| ***2nd*** | 1307.3 | *3rd* | 1297.2 | 2 | 0.77 | 0.18 | 93.4 | 5.24 | 0.99 | 0.06 | 0.10 | 0.02 | 0.01 |
| ***3rd*** | 1871.2 | *6th* | 1814.8 | 1 | 3.11 | 53.61 | 32.61 | 5.34 | 7.54 | 0.55 | 0.26 | 0.06 | 0.02 |
| ***4th*** | 2436.4 | *7th* | 2400.6 | 3 | 1.49 | 0.14 | 73.42 | 23.35 | 2.46 | 0.1 | 0.43 | 0.06 | 0.03 |
| ***5th*** | 3219.0 | *9th* | 3180.1 | 4 | 1.23 | 0.11 | 41.82 | 54.7 | 1.28 | 1.09 | 0.85 | 0.10 | 0.05 |
| ***6th*** | 3557.7 | *10th* | 3549.3 | 1 | 0.24 | 5.89 | 45.00 | 47.24 | 0.93 | 0.20 | 0.60 | 0.12 | 0.03 |
| ***7th*** | 3660.5 | *11th* | 3642.8 | 2 | 0.49 | 1.47 | 47.56 | 42.64 | 7.17 | 0.66 | 0.38 | 0.08 | 0.04 |
| ***8th*** | 3681.4 | *12th* | 3646.2 | 5 | 0.96 | 0.07 | 22.04 | 72.47 | 1.52 | 2.39 | 1.32 | 0.13 | 0.06 |
| ***9th*** | 4097.3 | *16th* | 4061.4 | 6 | 0.88 | 0.04 | 12.57 | 77.85 | 3.95 | 3.52 | 1.81 | 0.17 | 0.08 |
| ***10th*** | 4260.4 | *17th* | 4227.7 | 3 | 0.77 | 0.27 | 52.82 | 33.34 | 11.91 | 0.89 | 0.58 | 0.12 | 0.06 |

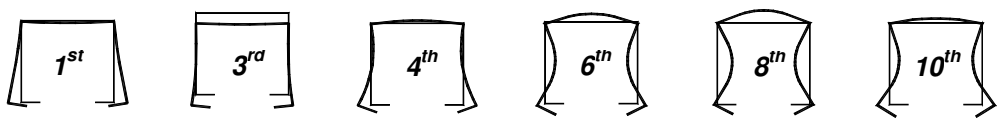


Figure 30: Mid-span cross-section deformed configurations of the ***1st***, ***3rd***, ***4th***, ***6th***, ***8th*** and ***10th*** vibration modes.

7.1.2 Dynamic response: periodic (sinusoidal) uniformly distributed load

The transverse displacement of the beam mid-web point $P$ (see fig. 29(a)), obtained through the superposition of its modal contributions, exhibits a sinusoidal time variation and is given by

$$w_P(t) = w_P^M \sin(\Omega t - \theta) \quad , \quad (11)$$

where $w_P^M$ and $\theta$ are the response amplitude and phase delay. Figures 31(a)-(b) show the corresponding $w_P^*-\Omega$ and $\theta-\Omega$ curves for the frequency range $0 \leq \Omega \leq 4000 rad/s$ – $w_P^* = w_P^M / w_P^0$ is the $w_P$ dynamic magnification factor and $w_P^0 = 0.178cm$ is the *static* displacement value. Curves obtained by means of GBT and ANSYS analyses are presented, and it is possible to observe the near coincidence between them. On the other hand, figure 32 provides the individual contributions to the $w_P^*-\Omega$ curve of the (i) **1st**, **3rd** and **6th** vibration modes, and (ii) GBT deformation modes **3**, **5** and **7**. The observation of the results presented in figures 31(a)-(b) and 32 prompts the following remarks:

(i) The $w_P^*-\Omega$ curve exhibits several well defined "peaks" ($P_1$-$P_5$ – $w_P^*$ tends to infinity) and "dips" ($P'_1$-$P'_4$ – $w_P^*$ tends to zero), corresponding to ($i_1$) *resonance* with the beam natural vibration modes and ($i_2$) *anti-resonance*, due to the cancellation of vibration mode contributions (in counter-phase).

(ii) The absence of a dip between $P_2$ and $P_3$, "compensated" by the existence of two consecutive ones between $P_3$ and $P_4$ ($P'_2$ and $P'_3$), is due to the negative amplitude of the **4th** vibration mode contribution (proportional to $-\sin(\Omega t - \theta)$). This means that the contributions of the **4th** and **6th** vibration modes, associated with the resonance frequencies of $P_3$ and $P_4$, are in phase with the dynamic load and, thus, $P'_2$ and $P'_3$ correspond to cancellations between the ($ii_1$) **3rd** and **4th**, and ($ii_2$) **3rd** and **6th** vibration mode contributions. Finally, one last word to mention that, as expected, one has $w_P(t) \equiv w_P^0$ (*i.e.*, $w_P^* = 1$) for $\Omega = 0$ – *i.e.*, when the load acts *statically*.

(iii) Figure 31(b) depicts the typical variation of the response phase delay $\theta$ with the loading frequency $\Omega$. Generally speaking, in the vicinity of a given *resonance frequency* $\omega_j$ one has ($iii_1$) $\theta = 0$ for $\Omega < \omega_j$ (in phase), ($iii_2$) $\theta = \pi$ for $\Omega > \omega_j$ (in counter-phase) and ($iii_3$) again $\theta = 0$ for $\Omega$ higher than the corresponding *anti-resonance frequency* that usually follows. The exception to this behaviour stems from the negative contribution of the **4th** vibration mode: for $\Omega > \omega_3$, $\theta$ rises initially from $0$ up to $\pi$, then rises again from $\pi$ to $2\pi$ and, finally falls back to $\theta = 0$ after the two consecutive anti-resonance frequencies.

(iv) There is an excellent qualitative agreement between the GBT and ANSYS $w_P^*-\Omega$ curves. Quantitatively speaking, such an excellent agreement is slightly "soiled" by a visible horizontal mismatch between the $P_2$ peaks, due to the *3.11%* difference between the $\omega_3$ values yielded by the two approaches (see table 1). Since the **3rd** vibration mode (associated with the $P_2$ peak) involves significant minor axis flexure, the above difference stems most likely from *shear lag* effects (not included in the GBT formulation employed).

(iv) Figure 32(a) shows the (expected) *regular* variation of the **1st**, **3rd** and **6th** vibration mode contributions to the beam response with $\Omega$. Each curve has a single peak, for $\Omega = \omega_j$, and then decays asymptotically to zero as $\Omega \rightarrow \infty$. The variation of the deformation mode **3**, **5** and **7** contributions, displayed in figure 32(b), are clearly *irregular*, due to the fact that more than one vibration mode is involved in each of them. Since they characterise

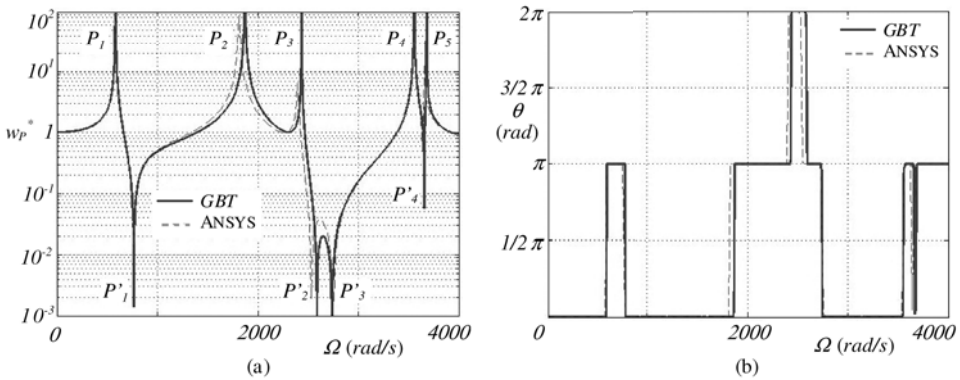


Figure 31: Variation of (a) $w_P^*$ (magnification factor) and (b) $\theta$ (phase delay angle) with $\Omega$ ($0 \leq \Omega \leq 4000 rad/s$).

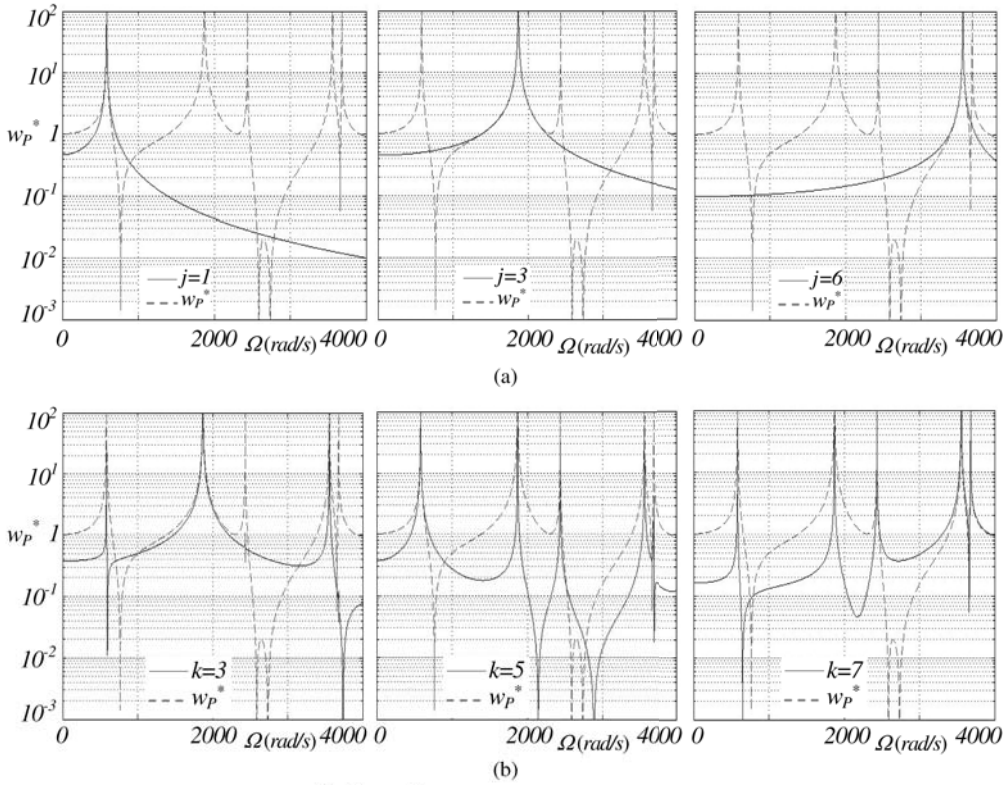


Figure 32: Contributions of the (a) ***1st*, *3rd*** and ***6th*** vibration modes and (b) GBT modes **3**, **5** and **7** to the $w_P^*$–$\Omega$ curve.

a specific structural behaviour (minor axis flexure, symmetric distortion or wall bending), several peaks may occur (when $\Omega$ equals a "participated" natural frequency), as well as dips (cancellation points). If a deformation mode $k$ is very predominant in a vibration mode $j$, its contribution to $w_P^*$ is close to the total value for $\Omega \approx \omega_j$ – *e.g.*, the contribution of mode **5** (predominant in the ***1st*** vibration mode) in the vicinity of peak $P_1$.

### 7.1.3 Dynamic response: moving point load

The results presented consist of static and dynamic *influence lines* concerning the vertical displacement of point $P$ (mid-span cross-section mid-web point – see fig. 29(b)). The beam response is again determined by superposing the vibration modes and the aim is to (i) assess the dynamic effects and (ii) investigate how the local (cross-section) deformations influence these effects. This last goal is achieved by performing two GBT analyses, (i) one including only deformation mode **3** (minor axis flexure) and (ii) the other involving all odd-numbered modes **3-17** ($n_d$=8).

Figure 33(a) show two static influence lines $A_P = w_P / w_P^{max}$ vs. $x/L$, where (i) $w_P^{max} \approx 0.102cm$ is the maximum displacement, corresponding to the point load acting at mid-span, and (ii) $w_P$ is the displacement caused by the point load acting at cross-section located at a distance $x$ from the beam left support. The two GBT-based curves concern (i) the total displacement (odd-numbered modes **3-17**) and (ii) only the flexural displacement (mode **3**) – they are compared with ANSYS shell finite element values and values yielded by classical beam flexural theory (BFT), respectively. Figure 33(b) provides the modal decomposition of the total displacement curve. One observes that:

(i) While the $A_P$ concerning the total displacement varies quite drastically for $3/8 \leq x/L \leq 5/8$, its flexural counterpart behaves quite "smoothly" and reaches a maximum for $A_P \approx 0.104$ – this means that local deformations account for nearly *90%* of $A_P$. Note also the very good agreement between the GBT results and the ANSYS and BFT values – maximum differences of *4%* and *0.1%*, respectively (occurring at mid-span).

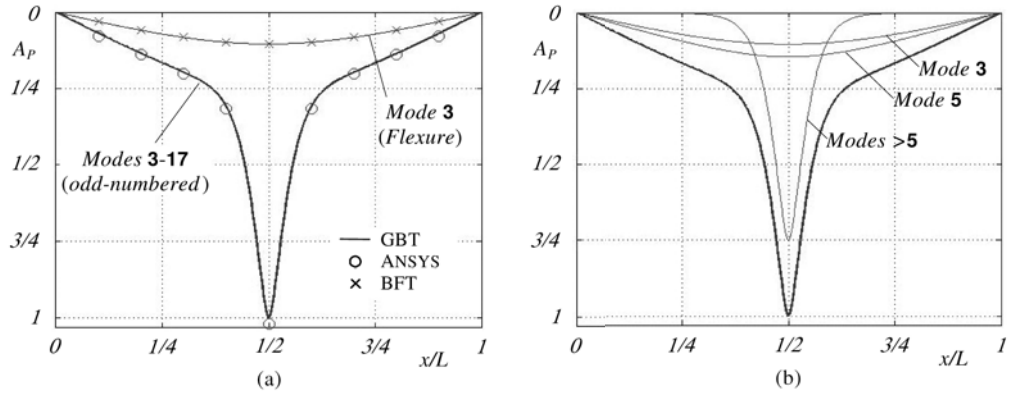


Figure 33: Beam static influence lines $A_P$ vs. $x/L$ (total and flexural displacement) concerning a point load: (a) comparison between GBT, ANSYS and BFT values, and (b) GBT modal decomposition (total displacement).

(ii) The drastic mid-span displacement increase for $3/8 \leq x/L \leq 5/8$ is due to *local deformations* (modes > **5**, mostly modes **7** and **9**). Indeed, while the contributions of modes **3** (flexure) and **5** (distortion) span the whole $x/L$ range, the local mode ones are practically null outside the $3/8 \leq x/L \leq 5/8$ range. Note also that the contributions of modes **3** and **5** are of the same order of magnitude, even if the latter is always a bit higher.

Figures 34(a)-(b) depict the *dynamic* influence lines $w_P^*$ vs. $x/L$, where $w_P^* = w_P / w_P^0$ and $w_P^0 \approx 0.102cm$ is the maximum static displacement) due to the moving point load, for (i) both flexural (Euler-Bernoulli) and total displacements, and (ii) various crossing frequencies $f = c/L$ ($f=0$ corresponds to the static influence lines shown in fig. 33(a)). It is worth noting that the free vibration behaviour taking place after the load has left the beam has not been considered (*i.e.*, the influences lines concern only the load *acting on* the bridge). All the influence lines were obtained by means of GBT analyses including (i) the odd-numbered deformation modes **3-17** and (ii) the first *10* vibration modes, characterised in table 1 – note that longitudinal symmetry no longer exists. For validation purposes, figure 34(b) also includes an influence line, concerning $f = 250\ s^{-1}$, that was obtained by means of an ANSYS shell finite element analysis – the moving load was modelled through the application of successive rectangular impulsive nodal loads along the beam "crossed path". These dynamic results lead to the following comments:

(i) The flexural dynamic influence lines exhibit the well-known evolution (*e.g.*, [35]): $w_P^*$ vs. $x/L$ ($i_1$) "oscillates" closely (small amplitude differences) about the static influence line, for low crossing speeds (*e.g.*,

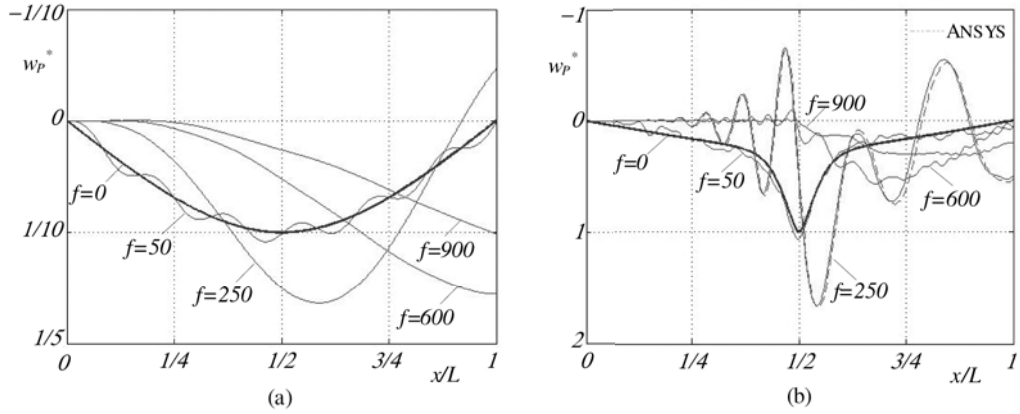


Figure 34: Beam dynamic influence lines $w_P^*$ vs. $x/L$ for crossing frequencies $f = 0, 50, 250, 600, 900\ s^{-1}$: (a) flexural and (b) total displacements (different vertical scales).

$f$=*50* $s^{-1}$), (ii) is "smooth" and exhibits a much higher maximum value when the load is well within the beam span, for intermediate speeds (*e.g.*, $f$=*250* $s^{-1}$), and (iii) is again "smooth" but exhibits its maximum value when the load leaves the beam, for high speeds (*e.g.*, $f$ >*600* $s^{-1}$). In the latter case, the maximum displacement drops as $f$ increases (recall that the free vibration behaviour occurring after the load exit was neglected) – $f$≈*600* $s^{-1}$ may be viewed as a "critical crossing speed", in the sense that the maximum displacement occurs exactly when the load is about to leave the beam. Note also the *slower* beam response as $f$ increases – $w_P^*$ remains practically null up to progressively higher $x/L$ values.

(ii) Due to the presence of distortional and (mostly) local deformation, the total deformation dynamic influence lines are much more irregular than their flexural counterparts. Nevertheless, they display similar qualitative features, even if the amplification levels are now much higher (note the different vertical scales in figs. 34(a) and 34(b)) – this fact provides clear evidence of the relevance of the cross-section in-plane deformation. Finally, note the virtual coincidence between the GBT and ANSYS $f$=*250* $s^{-1}$ influence lines.

## 8 CONCLUDING REMARKS AND FUTURE DEVELOPMENTS

This paper presented a state-of-the-art report on the most recent developments concerning formulations, numerical implementations and applications of GBT to analyse the structural response of thin-walled steel members and frames. Following an overview of the fundamental concepts and main procedures involved in the performance of the cross-section analysis, a unified view of the research activity recently carried out at IST (Technical University of Lisbon) was provided, namely by presenting brief accounts and illustrative examples for the various GBT formulations and numerical implemented (beam finite elements) developed in the last couple of years. In particular, the numerical results presented and discussed, aimed at showing the capabilities (numerical efficiency and structural clarity) of the novel GBT approaches, concern the local, distortional and/or global:

(i) First-order behaviour of steel-concrete composite beams and bridge decks ($i_1$) with cross-sections that combine closed cells with open branches and may include diaphragms (displacement restraints), and ($i_2$) acted by eccentric vertical loads. Shear lag effects were also taken into account, through the incorporation of specific deformation modes associated with non-linear (sinusoidal) warping along the steel flanges.

(ii) Buckling behaviour of members and frames subjected to complex loadings (namely those causing non-uniform internal force and moment diagrams) and exhibiting non-standard end and localised support conditions (*e.g.*, those modelling displacement restraints associated with bracing systems). Frames built from RHS members were also analysed (but subjected loadings causing only member axial compression).

(iii) Post-buckling behaviour of open-section beams subjected to non-uniform bending, exhibiting localised support conditions and containing critical-mode initial geometrical imperfections.

(iv) Post-buckling behaviour of frames built from open-section profiles, subjected to simple loadings (member axial compression only), exhibiting standard end support conditions (pinned, fixed or free end sections) and also containing critical-mode initial geometrical imperfections.

(v) Vibration behaviour of open-section members subjected to non-uniform internal force and moment diagrams and exhibiting standard end support conditions.

(vi) Dynamic behaviour of open-section members subjected to various loadings, such as a periodic uniformly distributed load or a point load moving along the member span.

For validation and computational efficiency assessment purposes, most the above GBT-based numerical results were compared with values yielded by shell finite element analyses performed in commercial codes (ADINA, ABAQUS and ANSYS). Despite the huge disparity between the numbers of degrees of freedom involved in the two analyses (orders of magnitude apart), an excellent agreement was invariably found. Moreover, the unique modal features of GBT make it possible to acquire in-depth insight on the mechanics of the structural problems investigated and, in some cases, unveil and/or shed new light on interesting phenomena. One must also stress the fact that *one-dimensional* beam models (but including folded-plate theory concepts) are able to provide accurate solutions for various 3D problems involving cross-section in- and out-of-plane deformations of prismatic thin-walled members and frames. For instance, it was possible to investigate in this paper aspects related to the:

(i) Influence of diaphragms located in specific composite bridge deck cross-sections.

(ii) Influence of the load position on the cantilever local, distortional and global buckling behaviour.
(iii) Buckling and post-buckling behaviour of members and frames with localised displacement restraints.
(iv) Relevance of including local deformations in the dynamic analysis of thin-walled members.

At this stage, it is also worth mentioning the recent development of a *preliminary version* of a GBT-based code to perform buckling and free vibration analyses of open-section single-span thin-walled members with various end support conditions and acted by non-uniform axial compression and/or bending moment diagrams. This code is designated GBTUL1.0$\beta$ [36] and can be freely downloaded from a TU Lisbon web page [37].

Before closing the paper, it is worth devoting a few words to mention work either currently under way or planned for the near future, concerning the development/implementation, application and dissemination of GBT formulations. It aims at covering the following (more or less specific) topics:

(i) Local, distortional and global dynamic behaviour of high-speed railway bridge decks – some results have already been reported [38].
(ii) First-order and buckling behaviour of steel-concrete composite structures including an improved concrete material modelling, namely by taking into account the non-linear effects due to cracking.
(iii) Buckling behaviour of plane and space frames acted by transverse loadings applied, taking into account ($iv_1$) localised effects associated patch loading and/or ($iv_2$) destabilising/stabilising effects stemming from the location of the load point of application within the cross-section (with respect to the shear centre).
(iv) Local, distortional and global post-buckling behaviour of plane and space frames built from open and closed-section members and exhibiting arbitrary loading and support conditions.
(v) Vibration and dynamic behaviour of plane and space thin-walled frames.
(vi) First-order, buckling and post-buckling behaviour of elastic-plastic thin-walled steel members and frames – in particular, the first step of this research effort will consist of trying to develop a "spatial plastic hinge approach".

Finally, one last word to inform that an upgraded version of the code GBTUL1.0$\beta$ [36, 37] will be made available in the near future. Besides correcting the bugs detected in the preliminary version, this second version will (i) have a friendlier graphical interface and (ii) cover members with arbitrary polygonal cross-sections, namely those combining closed cells with open branches. Moreover, the development of user-friendly and easy-to-use GBT-based numerical tools to analyse the fist-order and buckling behaviour of open and closed-section thin-walled steel frames is also planned for the not too distant future.

## ACKNOWLEDGEMENTS

The second author gratefully acknowledges the financial support of "*Fundação para a Ciência e Tecnologia*" (FCT – Portugal), through the post-doctoral scholarship nº SFRH/BPD/62904/2009.

## REFERENCES

[1] Schardt R., *Verallgemeinerte Technische Biegetheorie*, Springer-Verlag, Berlin, 1989. (German)

[2] Davies J.M. and Leach P., "First-order generalised beam theory", *Journal of Constructional Steel Research*, **31**(2-3), 187-220, 1994.

[3] Davies J.M., Leach P. and Heinz D., "Second-order generalised beam theory", *Journal of Constructional Steel Research*, **31**(2-3), 221-241, 1994.

[4] Schardt C., *Bibliographie zur VTB – Bibliograpy of the Generalized BeamTheory*, http://www.vtb.info/, 2001.

[5] Camotim D., Silvestre N., Gonçalves R. and Dinis P.B., "GBT analysis of thin-walled members: new formulations and applications", *Thin-Walled Structures: Recent Advances and Future Trends in Thin-Walled Structures Technology* (Loughborough, 25/6), J. Loughlan (ed.), Canopus Publishing, Bath, 137-168, 2004.

[6] Camotim D., Silvestre N., Gonçalves R. and Dinis P.B., "GBT-based structural analysis of thin-walled members: overview, recent progress and future developments", *Advances in Engineering Structures, Mechanics and Construction* (Waterloo, 14-17/5), M. Pandey, W.C. Xie, L. Xu (eds.), Springer, Dordrecht, 187-204, 2006.

[7] Camotim D., Basaglia C. and Silvestre N., "GBT buckling analysis of thin-walled steel frames: A state-of-the-art report", *Thin-Walled Structures*, 2010, in press.

[8] Bathe K.J., *ADINA System*, ADINA R&D Inc., 2003.

[9] Simulia Inc. *ABAQUS Standard*, version 6.7-5, 2008.

[10] Swanson Analysis Systems Inc., *ANSYS Reference Manual*, version 8.1, 2004.

[11] Silvestre N. and Camotim D., "First-order generalised beam theory for arbitrary orthotropic materials", *Thin-Walled Structures*, **40**(9), 755-789, 2002.

[12] Dinis P.B., Camotim D. and Silvestre N., "GBT formulation to analyse the buckling behaviour of thin-walled members with arbitrarily 'branched' open cross-sections", *Thin-Walled Structures*, **44**(1), 20-38, 2006

[13] Gonçalves R., Dinis P.B. and Camotim D., "GBT formulation to analyse the first-order and buckling behaviour of thin-walled members with arbitrary cross-sections", *Thin-Walled Structures*, **47**(5), 583-600, 2009.

[14] Silvestre N., "Generalised beam theory to analyse the buckling behaviour of circular cylindrical shell and tubes", *Thin-Walled Structures*, **45**(2), 185-198, 2007.

[15] Silvestre N., "Buckling behaviour of elliptical cylindrical shells and tubes under compression", *International Journal of Solids and Structures*, **45**(16), 4427-4447, 2008.

[16] Silvestre N. and Camotim D., "Non-linear generalised beam theory for cold-formed steel members", *International Journal of Structural Stability and Dynamics*, **3**(4)**,** 461-490, 2003.

[17] Gonçalves R., Ritto Corrêa M. and Camotim D., "A new approach to the calculation of cross-section deformation modes in the framework of generalised beam theory", *Computational Mechanics*, accepted for publication, 2010.

[18] Gonçalves R. and Camotim D., "Steel-concrete composite bridge analysis using generalised beam theory", *Steel & Composite Structures*, accepted for publication, 2010.

[19] Silvestre N. and Camotim D., "Local-plate and distortional post-buckling behavior of cold-formed steel lipped channel columns with intermediate stiffeners", *Journal of Structural Engineering* (ASCE), **132**(4), 529-540, 2006.

[20] Dinis P.B., Gonçalves R. and Camotim D., "On the local and global buckling behaviour of cold-formed steel hollow-flange channel beams", *Proceedings of 5th International Conference on Thin-Walled Structures* (ICTWS 2008 – Brisbane, 18-20/6), M. Mahendran (ed.), 425-432, 2008.

[21] Bebiano R., Silvestre N. and Camotim D., "Local and global vibration of thin-walled members subjected to compression and non-uniform bending", *Journal of Sound and Vibration*, **315**(3), 509-535, 2008.

[22] Camotim D., Silvestre N., Basaglia C. and Bebiano R., "GBT-based buckling analysis of thin-walled members with non-standard support conditions", *Thin-Walled Structures*, **46**(7-9), 800-815, 2008.

[23] Silva N.F., Camotim D. and Silvestre N., "Generalized beam theory formulation capable of capturing localized web buckling and load application effects", *Proceedings of 19th Specialty Conference on Cold-Formed Steel Structures*, (St. Louis, 14-16/10)**,** R. LaBoube, W.-W. Yu (eds.), 33-59, 2008.

[24] Basaglia C., *Non-Linear Analysis of Thin-Walled Steel Members and Frames Using Generalised Beam Theory*, Ph.D. Thesis, IST, Technical University of Lisbon, 2010. (Portuguese)

[25] Basaglia C. and Camotim D., "Buckling analysis of cold-formed RHS frames using generalised beam theory", *Proceedings of 13th International Symposium on Tubular Strucutures* (Hong Kong, 15-17/12), in press, 2010.

[26] Basaglia C., Camotim D. and Silvestre N., "Buckling behaviour of locally and globally braced thin-walled steel frames", *Proceedings of 6th International Conference on Advances in Steel Structures* (ICASS'09 – Hong Kong, 16-18/12), S.L. Chan (ed.), 891-890, 2009.

[27] Basaglia C., Camotim D and Silvestre N., "Non-linear GBT formulation for open-section thin-walled members with arbitrary support conditions", *Proceedings of 12th International Conference on Civil, Structural*

*and Environmental Engineering Computing* (CC 2009 – Funchal, 1-4/9), B. Topping *et al.* (eds), Civil-Comp Press, 21, 2009. (full paper in CD-ROM Proceedings)

[28] Basaglia C., Camotim D. and Silvestre N., "Non-linear GBT for thin-walled steel frames: formulation, implementation and application", *Proceedings of SSRC Annual Stability Conference* (Orlando, 12-15/5), 461-480, 2010.

[29] Basaglia C., Camotim D. and Silvestre N., "Local, distortional and global post-buckling analysis of frames using generalised beam theory", *Proceedings of 10th International Conference on Computational Structures Technology* (CST 2010 – Valencia, 14-17/9), in press, 2010.

[30] Basaglia C., Camotim D. and Silvestre N., "Non-linear GBT formulation for open-section thin-walled members with arbitrary support conditions", *submitted for publication,* 2009.

[31] Bebiano R., Silvestre N. and Camotim D., "Local and global vibration of thin-walled members subjected to compression and non-uniform bending", *Journal of Sound and Vibration*, **315**(3), 509-535, 2008.

[32] Bebiano R., Silvestre N., and Camotim D., "GBT-based dynamic analysis of thin-walled members", *Proceedings of 5th International Conference on Thin-Walled Structures* (ICTWS 2008 – Brisbane, 18-20/6), M. Mahendran (ed.), 1197-1210, 2008.

[33] Bebiano R., *Stability and Dynamics of Thin-Walled Members: Application of Generalised Beam Theory*, Ph.D. Thesis, IST, Technical University of Lisbon, 2010.

[34] Clough R.W. and Penzien J., *Dynamics of Structures* (2nd ed.), McGraw-Hill, New-York, 1993.

[35] Frýba L., *Vibration of Solids and Structures under Moving Loads* (3rd ed.), Thomas Telford, London, 1999.

[36] Bebiano R., Silvestre N. and Camotim D., "GBTUL – a code for the buckling analysis of cold-formed steel members", *Proceedings of 19th International Specialty Conference on Recent Research and Developments in Cold-Formed Steel Design and Construction* (St. Louis, 14-15/10), R. LaBoube, W.-W. Yu (eds.), 61-79, 2008.

[37] Bebiano R., Silvestre N. and Camotim D., *GBTUL 1.0β - Code for Buckling and Vibration Analysis of Thin-Walled Members*, freely available at http://www.civil.ist.utl.pt/gbt, 2008.

[38] Bebiano R., Silvestre N. and Camotim D., "Generalized beam theory-based local and global dynamic analysis of high-speed railway bridge decks", *Proceedings of 12th International Conference on Civil, Structural and Environmental Engineering Computing* (CC 2009 –Funchal, 1-4/9), B.H.V Topping *et al.* (eds.), Civil-Comp Press, 12, 2009. (full paper in CD-ROM Proceedings)